3D effects of strain vs. velocity weakening on deformation patterns in accretionary wedges

Jonas Bruno Ruh [a,*], Taras Gerya [b], Jean-Pierre Burg [a]

[a] ETH Zurich, Geological Institute, Sonneggstrasse 5, 8092 Zurich, Switzerland
[b] ETH Zurich, Institute of Geophysics, Sonneggstrasse 5, 8092 Zurich, Switzerland

ABSTRACT

Shear zones are weaker than surrounding rocks. Whether weakening depends on accumulated strain or strain rate is debated. We used a three-dimensional numerical code with a visco-plastic/brittle rheology to investigate the influence of strain and strain-rate weakening (often referred to as velocity weakening) on the evolution of thin-skinned fold-and-thrust belts. Two model setups are used: (i) a uniform setup to recognize the effects of each weakening mode on the structural evolution and dynamics of fold-and-thrust belts and (ii) a dual setup with two adjacent domains of décollement strength to investigate the structural response of laterally varying systems. Strain weakening and velocity weakening lead to remarkably different structural patterns. In particular, strain weakening favours out-of-sequence shear zones whilst some amount of finite plastic strain has to be achieved before the structural development initiates weakening. In contrast, velocity weakening starts with the onset of high strain-rate bands and does not favour out-of-sequence deformation. We also tested separately the influences of shortening velocity, cover sequence thickness and weakening style and amount on the structural evolution of the dual systems. The shortening velocity has a minor effect in strain-weakened models. Velocity weakening and a thinner cover sequence enhance the occurrence of strike-slip shear zones. We conclude that the weakening mode strongly influences the fault patterns and the dynamics of thrust wedges. Inversely, natural fault patterns are keys to discriminate weakening processes.

© 2014 Elsevier B.V. All rights reserved.

1. Introduction

Numerical modelling of accretionary wedges and thin-skinned fold-and-thrust belts has been an intense field of investigation using different techniques in two (e.g., Buiter, 2012; Buiter et al., 2006; Burbidge and Braun, 2002; Fillon et al., 2012; Miyakawa et al., 2010; Ruh et al., 2012; Simpson, 2011; Stockmal et al., 2007) and, more recently, in three dimensions (Braun and Yamato, 2010; Ruh et al., 2013). The simplest and most-often applied setup, like sandbox models (e.g., Konstantinovskaya and Malavieille, 2011), consists of a rectangular box that contains a thick layer of frictional material overlying a relatively weak and thin décollement layer. The bottom boundary is pulled out below the rigid walls, one of which represents the fixed backstop. This setup simulates a sequence of upper crustal rocks scraped off a subducting plate by the rigid backstop of a converging plate boundary. The advantages of this simple setup are (i) the comparability between models obtained with different analogue and numerical methods/codes, and (ii) its relevance to the analytical critical wedge theory (Dahlen, 1984; Dahlen et al., 1984; Davis and Engelder, 1985; Davis et al., 1983).

Mechanical studies of compressional thin-skinned fold-and-thrust belts often focus on the influence of décollement strength (Burbidge and Braun, 2002; Ruh et al., 2012), surface processes (Fillon et al., 2013; Selzer et al., 2007; Simpson, 2006), rheology of cover sequence and/or décollement (Ruh et al., 2012; Simpson, 2009), appearance of internal weak layers/inclusions (Ruh et al., 2012; Selzer et al., 2007; Stockmal et al., 2007; Yamato et al., 2011) and material cohesion (Nilfouroushan et al., 2012). Many of these studies applied a routine to weaken the modelled upper crustal layer, usually by decreasing the friction angle and/or cohesion of the corresponding plastic/brittle layer as a function of plastic finite strain (strain weakening). Few studies tested the effects of mechanical weakening on numerical wedges (e.g., Buiter et al., 2006; Ellis et al., 2004; Nilfouroushan et al., 2012; Selzer et al., 2007). According to Ellis et al. (2004), the amount of strain weakening and the strain threshold values above which weakening appears control the width, the abundance and the temporal development of shear zones. Selzer et al. (2007) supported this statement and showed that single shear zones due to strain weakening accommodate more displacement than shear zones in models without strain weakening.

In nature, several processes contribute to dynamic weakening of the lithosphere and to localization of high strain rate into narrow shear bands. These processes have been studied analytically as well as with analogue and numerical techniques. Examples for weakening processes are dynamic recrystallisation (e.g., Rutter, 1999), shear heating

* Corresponding author. Tel.: +41 44 632 88 17.
 E-mail addresses: jonas.ruh@erdw.ethz.ch (J.B. Ruh), taras.gerya@erdw.ethz.ch (T. Gerya), jean-pierre.burg@erdw.ethz.ch (J.-P. Burg).

(e.g., Burg and Schmalholz, 2008; Regenauer-Lieb et al., 2008; Thielmann and Kaus, 2012) and partial melting (e.g., Tumarkina et al., 2011), hydration metamorphism (e.g., Escartin et al., 1997), and grain-damage and -pinning (Bercovici and Ricard, 2012). These processes are essentially pertinent for deep crustal and mantle dynamics. They are implemented with non-physical routines (not based on a specific physical law), which depend on finite strain and/or strain rate (e.g., Allken et al., 2012; Lavier et al., 2000; Montesi and Zuber, 2003; Tackley, 2000). However, accretionary wedges and fold-and-thrust belts are for the most parts within the brittle regime of the crust, where modes of viscous weakening might not apply.

Two weakening processes are considered in upper crustal rocks: (i) lubrication of faults and shear zones and (ii) seismic dynamics. Evidence for fluid involvement in faulting and the consequent weakening effects has been argued in a wealth of studies (Hickman et al., 1995, and references therein; Stewart et al., 2000). It is well known that an increase in fluid pressure reduces the yield strength of brittle rocks (Fischer and Paterson, 1989). This is put forward for major décollements of accretionary wedges, where water-saturated shales form relatively weak horizons. High pore pressure may have different origins. On the one hand, layers containing pore fluids may be roofed and buried below impermeable sediments. With increasing overload, the pore space reduces as the dynamic pressure increases. Because the content in pore fluid remains constant, fluid pressure increases and weakens the rock. On the other hand, fluids can be released by diagenetic and metamorphic reactions such as the smectite to illite transition, which appears at ~2.5–5 km depth in clay-rich accretionary complexes and can account for up to 80% of the pore fluid (Bekins et al., 1994; Lanson et al., 2009). This input of additional fluid into an already water-saturated rock leads to fluid over-pressure and a decrease in rock strength. This would explain the low strength of deep décollement layers. The overlying rocks, though, have a lower pore-fluid pressure and are initially stronger than the basal décollement. During shortening of the sedimentary complex, brittle deformation develops fractures along which fluids can migrate through the formerly impermeable seal (Grando and McClay, 2007). The fracture is weakened by the locally increased fluid-pressure as soon as fluids infiltrate it. Mud volcanoes are exit ways and geological evidence of such over-pressured fluids escaping the accretionary system (e.g., Schluter et al., 2002). Since brittle failure occurs beyond a plastic threshold, fluids in faults can be considered to be strain-weakening components.

One of the main components, among others, to model long-term seismic processes is rate-dependent friction (e.g., Wang, 2007). In earthquake research, the dependence of rate (velocity) on friction has been discussed for several decades (Burridge and Knopoff, 1967; Dieterich, 1979; Ruina, 1983). Co-seismic slip-rate dependency of friction has been documented by rotary experiments (e.g., Di Toro et al., 2011) as well as in continuum visco-elasto-plastic numerical models (vanDinther et al., 2013). A rate-dependent friction within major fault zones was furthermore proposed by numerical and analytical calculations of Sleep (1995), who argued that increased fluid pressures and shear heating during earthquake activity weaken fault zones that are in long-term equilibrium with the country rock.

Lubrication and seismic weakening are both physically complicated and influenced by several processes. They can be differentiated by the manner frictional strength is weakened. In the case of fault lubrication, the rock strength is reduced by accumulated plastic strain. Fluids infiltrate a fault as soon as it appears (plastic strain increases), reduce the dynamic pressure of the infiltrated rock and thus lower its plastic yield strength. At variance, the seismic yield strength is rate dependent. In the following, strain rate-dependent weakening is described by the term "velocity weakening", emphasizing that velocity gradients are required for weakening.

We present different series of simulations to investigate the effects of strain vs. velocity weakening. Then, high resolution, three-dimensional models are used to test how structural coherence is maintained between two adjacent plastic/brittle wedges depending on different weakening properties. Models with a change in décollement strength are performed to understand three-dimensional effects of the different weakening styles. Especially, the evolution of transfer components, i.e. frontal fault bending or strike-slip faults, is investigated and compared to analogue modelling studies, where the development of transfer zones is also under intense debate (e.g., Bahroudi and Koyi, 2003; Calassou et al., 1993; Macedo and Marshak, 1999; Reiter et al., 2011). The formation and evolution of strike-slip systems have been extensively investigated with analogue modelling techniques (Dooley and Schreurs, 2012; and references therein). In compressional wedge models, shortening-parallel strike-slip faults can, for example, develop along transfer zones induced by lateral changes in indenter velocity (e.g., Reiter et al., 2011) or lateral variations sediment thickness (e.g., Marques and Cobbold, 2006). In analogue models with lateral variation of décollement resistance, the formation of strike-slip faults depends on the strength contrast between the different décollements (Graveleau et al., 2012). We evaluate our results in the context of the analytical critical wedge theory and shortly present their relevance to geological examples of fold-and-thrust belts.

2. Model setup

The numerical model is similar to that documented and used in an earlier study (Ruh et al., 2013). It is based on a three-dimensional, high-resolution, fully staggered grid, finite difference, marker in cell model with a standard visco-brittle/plastic rheology and an efficient OpenMP-parallelized multigrid solver (Gerya, 2010; Gerya and Yuen, 2007). Governing equations and their numerical implementation are specified in Appendix A.

2.1. Geometrical setup and material properties

Model setups of all simulations are constructed on Eulerian grids dimensioned to account for different requirements: vertical thickening of the wedge, possible lateral structural changes throughout the evolving wedge and increasing length of the wedge while the wedge front migrates. The planar backstop is defined by a vertical grid boundary with zero horizontal velocity. High resolution allows the development of high strain-rate shear bands sufficiently narrow (1–2 cell widths) to be comparable to natural fault systems. We present two series of simulations. The first series uses a geometrically uniform setup (series U) with geometry and rheology being equal over the whole model. Small but negligible disparities in results are due to the initially random distribution of Lagrangian markers within the Eulerian grid and variations along strike are negligible. These models were performed to compare results with (i) the two dimensional critical wedge theory (Dahlen, 1984; Dahlen et al., 1984; Davis et al., 1983) and (ii) earlier, two-dimensional numerical studies (e.g., Ellis et al., 2004; Selzer et al., 2007). Series U shows the structural and dynamic repercussions of strain vs. velocity weakening. The second series incorporates two halves with different décollement strength (series D). The sharp, vertical boundary at $L_y = 50$ km (Fig. 1b) is contained in the décollement layer, parallel to the shortening direction (x-axis).

Eulerian grid dimensions of series U models are 150 · 50 · 20 km in x-, y-, z-directions with a nodal resolution of 309 · 85 · 149, respectively; the resulting cell size is 487/595.2/135.1 m in x-, y-, z-directions (Fig. 1a). Series D models are prescribed to structurally vary laterally (y-direction) and therefore have a wider setup. The dimension of the Eulerian grid is 100 · 100 · 20 km with a resolution of 245 · 245 · 149 in x-, y-, z-directions, respectively. The resulting cell size is 409.8/409.8/135.1 m in x-, y- and z-directions (Fig. 1b). Lagrangian marker resolution for both series is two markers per cell in every direction. This setting results in a resolution of 8.9 million nodes with about 70 million Lagrangian markers for models with the highest resolution.
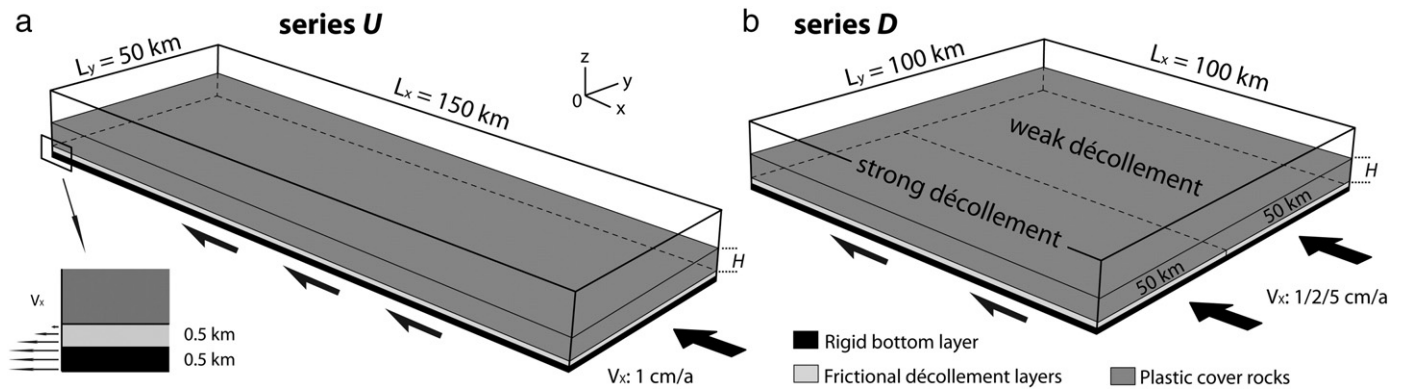
Fig. 1. Model setup. Black: 500 m thick rigid plate entering and exiting the Eulerian grid. Light grey: 500 m thick frictional décollement layer. Grey: brittle/plastic cover sequence with thickness H. Bottom left: treatment of velocity at the backstop boundary. a) Uniform models (series U). V_x = 1 cm/a. b) Laterally varying simulations (series D). V_x = 1, 2 or 5 cm/a. Décollement strength varies over width.

Material properties are initially defined on the Lagrangian markers, which are advecting through the Eulerian grid. From bottom to top of the Eulerian grid, marker types are distributed as follows: a 500 m thick rigid plate is the bottom. Uniform models have a basal strength defined by a friction angle of $\varphi_b = 10°$. Weak and strong basal strengths in dual models are given by friction angles of $\varphi_b = 5°$ and $15°$, respectively (Fig. 1). Above the rigid plate, the 500 m thick décollement horizon with a frictional rheology soles a "sedimentary" layer. Uniform models exhibit a cover sequence thickness of $H = 5$ km, dual models are run with $H = 2.5$ and 5 km (Fig. 1). Density is 2700 kg/m³ for the lower rigid plate, the décollement and the sediment layer in all models of this study. Initial viscosity of all rock types is 10^{23} Pa·s. Lower and upper cutoff viscosities are 10^{18} Pa·s and 10^{23} Pa·s, respectively. Other material parameters are listed in Table 1. Simulation parameters of series U are given in Table 2, parameters of series D in Table 3.

All Lagrangian markers above the plastic "sediments" are defined as "sticky-air", an approach that mimics a quasi-free surface (Crameri et al., 2012; Gerya and Yuen, 2003; Schmeling et al., 2008; Zaleski and Julien, 1992). The low density (1 kg/m³) and small viscosity (10^{18} Pa·s) of the sticky-air layer ensure sufficiently small normal stresses at the sediment surface. Analytical predictions have been made for a similar setup to test the quality of this free-surface approach (Ruh et al., 2013). They showed that it fulfils the general condition for a traction-free surface.

2.2. Boundary conditions

A velocity V_x is defined at the lower ($z = 0$ km) and frontal boundaries ($x = L_x$; Fig. 1), which is equivalent to pulling out the bottom sheet of a sand box model below a rigid backstop (e.g., Konstantinovskaya and Malavieille, 2011). New Lagrangian marker layers coming in through the front side allow large deformation. The back side of the setup ($x = 0$ km) acts as backstop with a no-slip boundary condition. At the bottom, the 500 m thick

rigid plate of high constant viscosity is included; it allows a better stability of the multigrid solver at the lower model boundary. Between the bottom rigid plate and the "backstop", the 500 m thick décollement undergoes simple shear (V_x at $z = 500$ m to 0 cm/a at $z = 1000$ m; Fig. 1). Both lateral boundary conditions (at $y = 0$ km and $y = L_y$) are defined as free slip along the boundary planes. An upward velocity is applied at the upper boundary. This balances the volume of exiting "sticky-air" markers and the volume of incoming material at the front boundary to fulfil the conservation of volume.

2.3. Strain weakening

Strain induced by plastic deformation is accumulated every time step and stored on every marker. Strain weakening is modelled as a linear decrease of frictional angle and/or cohesion between accumulated plastic strains of $\varepsilon_w{}^0 = 0.5$ and $\varepsilon_w{}^1 = 1.5$ (Fig. 2a). These lower and upper thresholds of strain for weakening activation and completion are similar to those in previous numerical investigations of strain weakening of crustal rocks (e.g., Allken et al., 2012; Huismans et al., 2005; Selzer et al., 2007; Stockmal et al., 2007). How the amount of strain weakening (φ_w) influences the structural and the overall wedge shape is investigated in U series, uniform simulations. Series D models with strain weakening focus on the relationships between the amount of strain weakening (φ_w), the thickness of "sediment" (H) and the shortening velocity (V_x). Our code has no healing term as in other codes (e.g., Gerya, 2013; Tackley, 2000), so that weakened material does not strengthen again.

2.4. Strain-rate weakening

Velocity weakening is computed like strain weakening. The friction angle and cohesion are lowered to a weakened value (φ_w, C_w) when strain rate is exceeding a critical value. In contrast to the strain-weakening routine, weakening does not increase linearly between two strain rates, but depends only on one threshold strain rate, $\dot{\varepsilon}_w$, above which weakening is activated (Fig. 2b). The effect of strain-rate- or velocity-dependent weakening has been tested in several studies and has been compared to a linked strain-weakening/healing system (e.g., Bercovici, 1993; Tackley, 1998). It is argued that the strengthening due to a decrease of strain rate has a similar effect as strain-rate healing of weakened zones, where the healing strain rate is multiplied with the numerical time step and then subtracted from the accumulated strain. Series U simulations with velocity weakening are all weakened to equal values (φ_w, C_w) but controlled by different threshold strain rates $\dot{\varepsilon}_w$ (Table 2; UV models). Series D simulations are conducted with different weakening (φ_w), sediment thickness (H) and shortening velocity (V_x) (Table 3; DV models).

Table 1
Parameter definition.

Parameter	Meaning
φ_0	Initial friction angle
φ_w	Weakened friction angle
C_0	Initial cohesion
C_w	Weakened cohesion
ε_w	Weakening strain
$\dot{\varepsilon}_w$	Weakening strain-rate
φ_b	Décollement friction angle
κ	Diffusion constant
H	Rock sequence thickness
V_x	Shortening velocity

Table 2
Parameters of uniform simulations.

Simulation	φ_0 (°)	φ_w (°)	C_0 (MPa)	C_w (MPa)	$\varepsilon_w^{0.1}$ (−)	φ_b (°)	κ (m/s²)	H (m)	V_x (cm/a)	Figure
US1	30	10	20	0.2	0.5–1.5	10	10^{-12}	5000	1	3
US2	30	15	20	0.2	0.5–1.5	10	10^{-12}	5000	1	3, 16
US3	30	20	20	0.2	0.5–1.5	10	10^{-12}	5000	1	3, 9
US4	30	25	20	0.2	0.5–1.5	10	10^{-12}	5000	1	3
US5	30	30	20	0.2	0.5–1.5	10	10^{-12}	5000	1	3
US6	30	30	20	20	0.5–1.5	10	10^{-12}	5000	1	3
US7	30	20	20	0.2	0.5–1.5	10	10^{-20}	5000	1	8
US8	30	20	20	0.2	0.5–1.5	10	10^{-6}	5000	1	8

Simulation	φ_0 (°)	φ_w (°)	C_0 (MPa)	C_w (MPa)	$\dot{\varepsilon}_w$ (s⁻¹)	φ_b (°)	κ (m/s²)	H (m)	V_x (cm/a)	Figure
UV1	30	15	20	0.2	10^{-13}	10	10^{-12}	5000	1	6
UV2	30	15	20	0.2	$3.3 \cdot 10^{-14}$	10	10^{-12}	5000	1	6, 16
UV3	30	15	20	0.2	10^{-14}	10	10^{-12}	5000	1	6
UV4	30	15	20	0.2	$3.3 \cdot 10^{-15}$	10	10^{-12}	5000	1	6

Both, strain- and velocity-weakening limits are grid step-size dependent and are scaled to the respective amount of displacement and rate of displacement along the spontaneously forming faults (e.g., Gerya, 2013; Lavier et al., 2000; vanDinther et al., 2013).

2.5. Surface processes

A routine is implemented to mimic sedimentation in piggy-back, surface depressions. The surface between "rocks" and "sticky-air" markers defines the apparent topography. The way the exact topography is obtained, independent of the nodal resolution, is described in Ruh et al. (2013). To simulate surface process, the topography surface is diffused at every timestep depending on its local 2D curvature:

$$\frac{\partial h_s}{\partial t} = \kappa \cdot \frac{\partial^2 h_s}{\partial x_i^2} \tag{1}$$

where κ is the diffusion constant, h_s the surface topography and x_i the spatial coordinates ($x_1 = x$, $x_2 = y$). The diffusion constants applied in the presented simulations are listed in Tables 1 and 2. The topography diffusion equation was solved implicitly on one thread using the direct solver PARDISO (Schenk and Gartner, 2004, 2006).

To address deposition without erosion, markers with a "sticky-air" rheology below the updated surface transmute to "rock" rheology with an accumulated plastic strain value of zero. Markers with "rock" rheology above the updated surface remain unchanged. The intensity of topography diffusion is low in most simulations and mainly aims to preclude overthrusting of low-viscosity "sticky-air" markers at the model surface, which may produce non-physical intrusion of "sticky-air" into spontaneously forming thrust zones. One set of simulations was conducted to investigate the influence of sedimentation on the structural evolution of the wedge by applying different diffusion constants (US3,7,8; Table 2).

Surface slopes of developing wedges have been calculated by linear regression. Only surface elevations 100 m higher than their initial value have been considered to discount the flat fore-wedge that has not yet been incorporated into the wedge.

3. Results

Results from simulations with uniform and dual setups and with either strain- or velocity-dependent weakening of the numerical wedges are presented separately. Deformation was initiated along the backstop in all simulations.

3.1. Uniform models (U series)

Twelve uniform simulations are presented (Table 2). They all show negligible lateral variations due to randomness of Lagrangian markers, as mentioned. Therefore, results of series U simulations are presented in the form of two-dimensional profiles across the middle width ($y = 25$ km) of the 50 km wide models. A three-dimensional view of a typical simulation is given as Supplementary material (model US3; Table 2).

3.1.1. Strain-weakening uniform models (US models)

Results of uniform models with weakening depending on finite plastic strain with a wide range of internal friction angles and cohesions are presented in Fig. 3. Two points deserve emphasis: (i) The larger the amount of weakening, (i.e. the lower fully weakened friction angle φ_w), the steeper the surface taper, and (ii) shear zones have larger offsets in models with greater weakening (Fig. 3a). The surface tapers of our model match the theoretical minimum calculated with the critical wedge theory, taking the fully weakened values (φ_w, C_w) for internal strength (Fig. 3a). The effect of internal wedge strength on critical tapers is illustrated with a flounder diagram; minimum and maximum critical
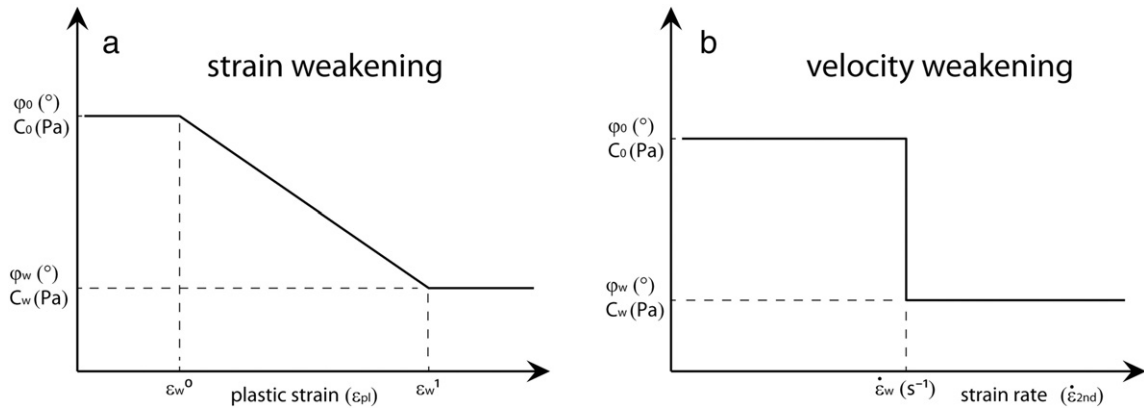
Table 3
Parameters of dual simulations.

Simulation	φ_0 (°)	φ_w (°)	C_0 (MPa)	C_w (MPa)	$\varepsilon_w^{0.1}$ (−)	φ_b (°)	κ (m/s²)	H (m)	V_x (cm/a)	Figure
DS1	30	10	20	0.2	0.5–1.5	5/15	10^{-20}	5000	1	10
DS2	30	20	20	0.2	0.5–1.5	5/15	10^{-20}	5000	1	10, 11
DS3	30	20	20	0.2	0.5–1.5	5/15	10^{-20}	5000	5	11
DS4	30	20	20	0.2	0.5–1.5	5/15	10^{-20}	2500	2	13, 17
DS5	30	20	20	0.2	0.5–1.5	5/15	10^{-20}	2500	5	13
DS6	30	30	20	0.2	0.5–1.5	5/15	10^{-20}	5000	1	10

Simulation	φ_0 (°)	φ_w (°)	C_0 (MPa)	C_w (MPa)	$\dot{\varepsilon}_w$ (s⁻¹)	φ_b (°)	κ (m/s²)	H (m)	V_x (cm/a)	Figure
DV1	30	20	20	0.2	$3.3 \cdot 10^{-14}$	5/15	10^{-20}	5000	1	14, 17
DV2	30	20	20	0.2	$3.3 \cdot 10^{-14}$	5/15	10^{-20}	5000	5	14
DV3	30	20	20	0.2	$3.3 \cdot 10^{-14}$	5/15	10^{-20}	2500	2	15
DV4	30	20	20	0.2	$3.3 \cdot 10^{-14}$	5/15	10^{-20}	2500	5	15, 17

Fig. 2. Plastic weakening behaviour of material. a) Strain weakening is initiated after reaching an accumulated plastic strain $\varepsilon_w{}^0$. Then, initial friction angle and cohesion (φ_0, C_0) both linearly decrease between $\varepsilon_w{}^0$ and $\varepsilon_w{}^1$ to the weakened values (φ_w, C_w), which they keep. b) Velocity weakening instantaneously lowers the frictional strength from φ_0, C_0 to φ_w, C_w when reaching the threshold strain rate $\dot{\varepsilon}_w$. Unlike strain, strain rates can decrease and material is strengthened again to its initial values if strain rates fall below the critical value $\dot{\varepsilon}_w$.

tapers delimit the area of wedge stability (Fig. 4a). For identical décollements, the minimum critical tapers are lower for stronger wedges. The stable wedge area is smaller for internally weaker wedges. If the internal strength of the wedge is equal to that of the décollement, the wedge has no stable area and minimum and maximum critical tapers are identical (Fig. 4a). Surface slopes of simulations US1–5 have been plotted after a run time equivalent to 3 and 6 Ma, depending on their post-weakening strength (Fig. 4b). After 3 Ma all simulations reached their minimum critical taper. After 6 Ma, most of the wedge tapers plot within the stable zone, except model US1, which theoretically has no stable area (Fig. 4).

Accumulated plastic strain after 11.5–11.6 Ma of models US1–6 show that deformation is more diffuse in wedges with less weakening (Fig. 3b). Conversely, strain in strongly weakened models (e.g. US1–3) is localized into shear zones, including short-lived, backward-verging shear zones that delimit pop-up structures during frontal accretion of a new thrust sheet (Fig. 3b). Such structures are not seen in less weakened models like US4–6, in which strain distribution is diffuse. Comparing models US5 and 6 discloses the influence of cohesion on shear zone development. Although the angle of the taper is similar, the development of localized shear zones with increased strain is clearly enhanced when internal cohesion is weakened (Fig. 3b).

Viscosity and plastic strain are stored on every marker throughout the modelling process. Every "sediment" marker with a viscosity lower than its initial value of 10^{23} Pa·s can be considered to be plastically failed, according to the viscous formulation of the plasticity-law used in this study. In the following, we consider a marker to be strongly failed if its viscosity is $<10^{22}$ Pa·s, the value that brings stresses down to yield stresses. Dynamics of the strain-weakened simulations are further investigated by looking at the strain rate of failed and strongly failed markers after ~10 Ma run time in each model (Fig. 5).

For simulation US1, about 25% of all sediment markers are at failure ($\eta < 10^{23}$ Pa·s) with a dominant strain rate of ~10^{-15} s^{-1} (Fig. 5a). Around 10% of these markers classify as strongly failed ($\eta < 10^{22}$ Pa·s) with a dominant strain rate of ~$2 \cdot 10^{-14}$ s^{-1}. With large fully weakened friction angles φ_w, i.e. reduced weakening, several observations stand out: (i) the percentage of failed markers within the wedge increases from about 25% (model US1; Fig. 5a) to about 45% (model CS6; Fig. 5f); (ii) the percentage of strongly failed markers decreases from ~10% in US1, to ~6% in US6; and (iii) the spectrum of strain rate in failed markers becomes narrower for models with less weakening. A small amount of failed markers of model US1 has strain rates of $<10^{-16}$ s^{-1} and $>10^{-13}$ s^{-1} (Fig. 5a). Strain-rate values for failed markers in model US6 range all between 10^{-16} s^{-1} and 10^{-13} s^{-1} (Fig. 5f).

The temporal development of accumulated plastic strain within strain-weakened models reveals that weakening is especially efficient if the friction angle is sufficiently lowered (Fig. 5a–c). The small

percentage of markers between plastic strains of $\varepsilon_w{}^0 = 0.5$ and $\varepsilon_w{}^1 = 1.5$ indicates that weakened markers ($\varepsilon_{pl} > 0.5$) accumulate strain very fast to become fully weakened ($\varepsilon_{pl} > 1.5$). Strain rate, and therefore strain, is not localized in models where weakening does not reduce the friction angle (Fig. 5e,f).

3.1.2. Velocity-weakening uniform models (UV models)

Simulations including velocity weakening are presented in Fig. 6. Wedge deformation after a run time of ~10 Ma indicates that there are fewer shear zones in models where weakening is more difficult, i.e. the thresholds of φ_w and C_w are higher (Fig. 6a). In general, spacing between shear zones is larger and shear zones dip with lower angles towards the backstop than in strain-weakened models (Fig. 6a). For weakening thresholds of 10^{-13} s^{-1} (model UV1) and $3.3 \cdot 10^{-14}$ s^{-1} (model UV2), thrust sheets construct a classical imbricate fan type wedge. Backstop-verging shear zones occur for low strain-rate thresholds (model UV3; Fig. 6a). In contrast to backstop-verging or out-of-sequence shear zones in strain-weakened simulations, a strongly strained rear, close to the backstop boundary, is another remarkable feature of models with low weakening thresholds. "Sediments" have thickened and rotated, dipping towards the trench (e.g. model UV4; Fig. 6a). In fact, these strained rears result from the vertical shear zone along the backstop boundary, which contributes to local uplift.

All velocity-weakened simulations have in common that ramp anticlines developing at the wedge toe collapse. The collapsed and deposited material is illustrated by increased plastic strain in depressions between thrust sheets (Fig. 6b). Ramp shear bands predominantly proceed below such trench fillings. Surface slopes of velocity-weakened simulations in function of strain threshold reveal two trends: (i) the larger the weakening threshold, the flatter the tapers and (ii) surface slopes decrease with increasing run time (Fig. 7). All surface slopes lay above the theoretical critical minimum taper calculated with an internal friction angle of $\varphi = 15°$.

Strain-rate distribution of failed and strongly failed markers after ~10 Ma run time varies strongly with weakening thresholds (Fig. 8). For model UV1 ($\dot{\varepsilon}_w = 10^{-13}$ s^{-1}) 22% of cover Lagrangian markers are at failure (Fig. 8a). The failed markers dominantly deform with a strain rate slightly below 10^{-15} s^{-1}, whereas strongly failed markers reach very high strain rates up to 10^{-12} s^{-1}. Strain rates are less focussed with smaller velocity-weakening thresholds (Fig. 8b,c). For $\dot{\varepsilon}_w = 3.3 \cdot 10^{-15}$ s^{-1}, only about 6% of "sediment" markers are at failure, half of them being strongly failed (Fig. 8d). Strain rates of strongly failed markers show a slight peak at the very largest strain rates for all models of series UV (Fig. 8). Generally, strain-rate peaks of failed markers (~10^{-15} s^{-1}) refer to non-weakened rocks in all velocity-weakened models. Most of the strain rates of strongly failed markers ($>\dot{\varepsilon}_w$; except for model UV1) represent frictionally weakened zones.
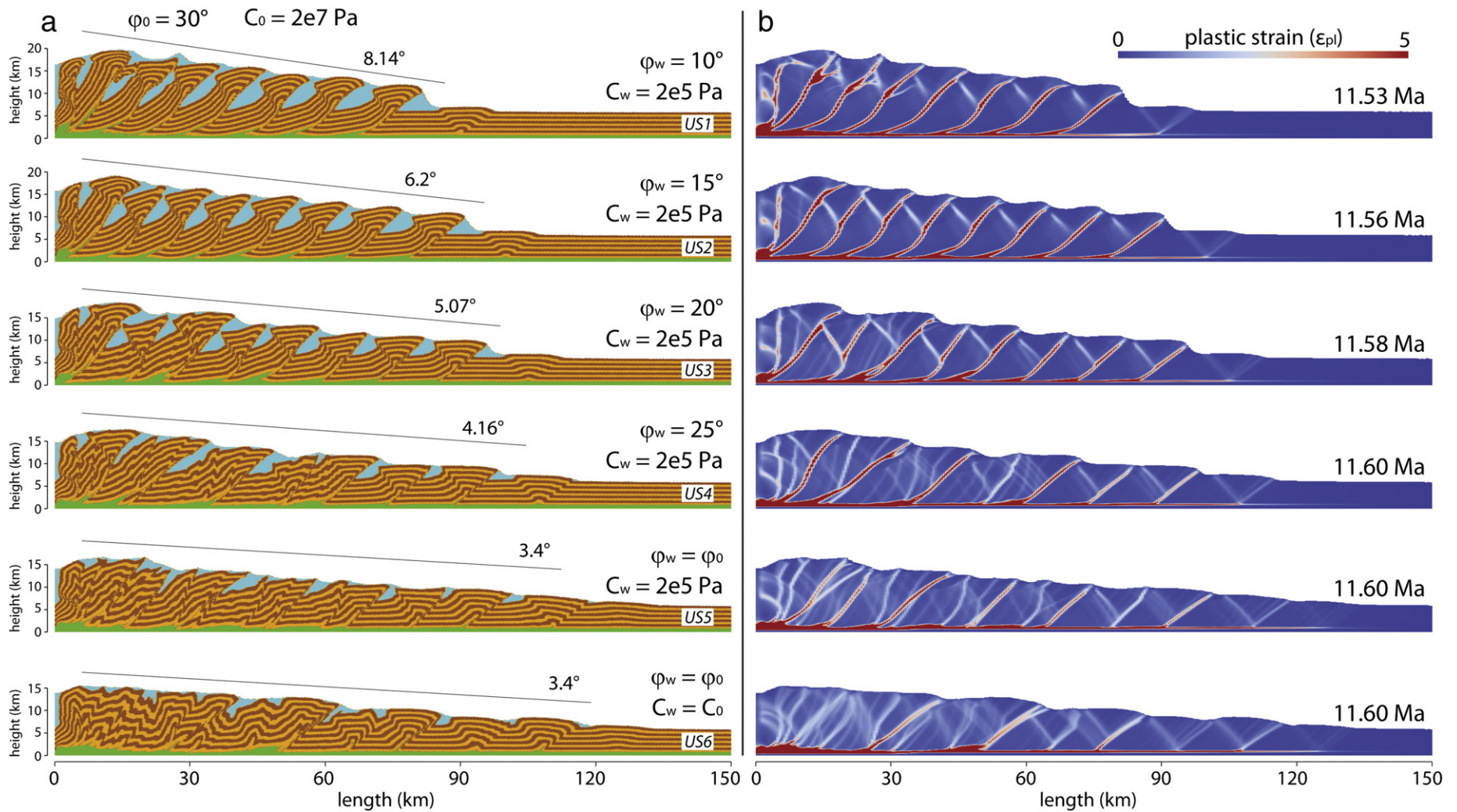
Fig. 3. Profiles at $y = 25$ km across uniform simulations after 11.5–11.6 Ma with decreasing amounts of strain weakening from top to bottom. a) Deformed strata inferred from Lagrangian markers. Green: basal décollement. Brown and beige: sediment; different colours are visualisation passive markers with no rheological differences. Blue: sediments added in surface depression. Solid lines: analytical surface slopes calculated with weakened internal strength. b) Accumulated plastic strain (same colour scale, on top, for all profiles).
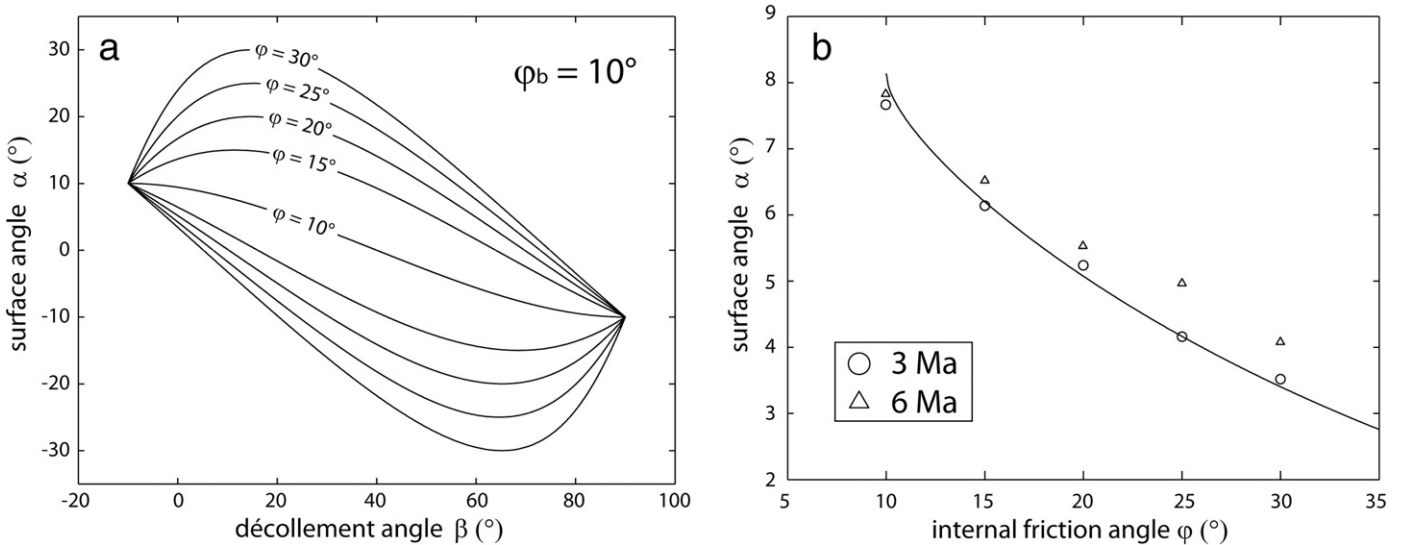
Fig. 4. a) Flounder diagrams defining minimum and maximum critical tapers for wedges with a basal friction angle $\varphi_b = 10°$ and internal friction angles $\varphi = 10$–$30°$. b) Analytical test of strain-weakened uniform wedges. Solid line: theoretically derived minimum critical taper. Circles: surface slopes calculated by linear regression at $y = 25$ km after 3 Ma run time. Triangles: same profile after 6 Ma run time.

3.1.3. Effect of sedimentation

Simulations differing only in their surface diffusion constant κ were conducted to test the effect of sedimentation on the structural and mechanical evolution of wedges (Fig. 9). As most of known accretionary wedges are sub-marine (Morley et al., 2011), erosion was not implemented. In general, the volume of sediments filling piggy-back style basins increases with increasing surface diffusion constant. If surface processes are kept low ($\kappa = 10^{-20}$ m/s²), thrust sheets are stacked with little intervening sedimentary material (Fig. 9a). Vertical offset components of shear zones are roughly equal to the sediment thickness. For intermediate sedimentation rates ($\kappa = 10^{-12}$ m/s²), shear zone offsets are similar to offsets in low sedimentation simulations, whereas shear zone spacing increases (Fig. 9b). For high sedimentation rates ($\kappa = 10^{-6}$ m/s²), shear zones exhibit larger offsets than in lower sedimentation simulations and thrust spacing is further increased (Fig. 9c). This widening of thrust spacing is induced by the additional load from more sedimentation in front of the wedge, which locally increases the wedge strength. The consequence is to shift the deformation front further away from the rear. Tapers of all simulations are roughly equal and consistent with the critical wedge theory (Fig. 9).

3.2. Dual models (D series)

Ten simulations with a linear discontinuity in décollement strength parallel to the shortening direction are presented (Table 3). The difference in décollement strength is the same in all models: the basal décollement is strong (friction angle $\varphi_b = 15°$) from 0 to 50 km in y-direction and weaker (friction angle $\varphi_b = 5°$) from 50 to 100 km (Fig. 1b). Models differ in the amount of strain weakening, the shortening velocity and the sediment thickness to investigate how these parameters influence the development of a transfer zone.

3.2.1. Strain-weakening models (DS models)

3.2.1.1. Sediment thickness H = 5 km.
Three simulations with different weakening values of the wedge after a run time of ~4 Ma illustrate the influence of strain weakening along the separation between the décollement halves (Fig. 10). If the wedge internal friction angle is reduced from $\varphi = 30°$ to $\varphi_w = 10°$ (model DS1), the surface trace of the frontal thrust is everywhere sub-parallel to the backstop (Fig. 10a). Topography of the rear of the model varies, higher surface

elevations standing above the stronger half of the décollement. The deformed wedge at $y = 0$ and $y = 100$ km displays different deformation styles (Fig. 10a; black and white in the topography plots). Above the weak décollement ($y = 100$ km), an imbricate thrust fan looks like that obtained in the uniform models (Fig. 3a). Above the strong décollement ($y = 0$ km), thrust sheets are more disturbed, especially by a normal shear zone dipping shallowly towards the wedge toe (Fig. 10a). The evolution of this normal shear zone strongly influences the surface slope of the wedge. The fact that the highly strained "sediment" is weaker than the underlying décollement leads to a repose angle equal to the minimum critical taper (no stable wedge area; Fig. 4a).

Surface slopes are investigated at 25 and 75 km of the y-axis, the mid-widths of each wedge part. The temporal evolution of the surface slope at $y = 25$ km shows strong oscillations above and below the minimum critical taper. Surface slope is there slightly lower while the slope atop the weak base ($y = 75$ km) is slightly larger than the analytical value (Fig. 10a).

For a smaller weakened friction angle ($\varphi_w = 20°$; model DS2), topographic peaks are lower than in model DS1 (Fig. 10b). This is consistent with the critical wedge theory (Fig. 4). The trace of the frontal shear zone is curved above the boundary between weak and strong décollements. Structurally, the wedge above the relatively weak base develops thrust imbrication dominantly dipping towards the backstop. Atop the strong base, the leading imbricate fan has less shear zones that each absorbs larger displacements than shear zones in the other half of the model (Fig. 10b). As seen in the uniform models, wedges are generally flatter for smaller strain weakening (Fig. 3). Surface slopes along profiles at $y = 25$ and 75 km indicate that tapers of the wedge initially exceed and subsequently decrease towards the theoretical minimum critical taper (Fig. 10b). Tapers are relatively steep after ~1 Ma, because only one thrust sheet is contributing to the calculated surface slope.

The wedge exhibits a relatively low surface elevation if only internal wedge cohesion is decreased while the internal friction angle remains constant (Fig. 10c; model DS6). Migration of the wedge toe above the weak décollement is not defined by shear zones since deformation remains diffuse. Atop the strong base, out-of-sequence shear zones cut through the earlier leading imbricate fan (Fig. 10c). Low elevations go hand in hand with low surface slopes. Like in model DS2, surface slopes of both parts initially exceed the theoretical minimum taper and then decrease towards the critical value (Fig. 10c).
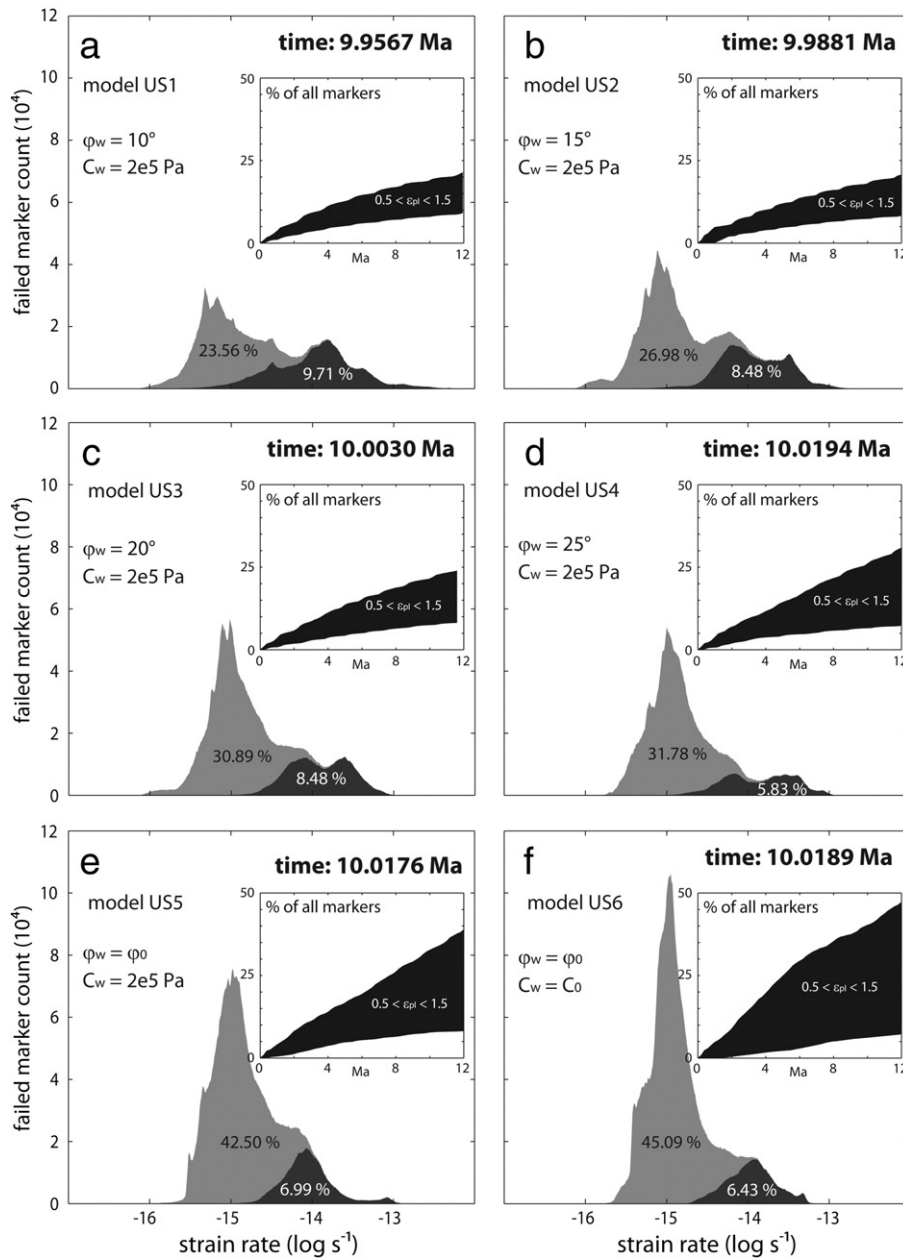
Fig. 5. Strain-rate distribution of plastically yielded Lagrangian markers within the wedge of simulations US1–6 with different amounts of strain weakening after ~10 Ma run time. Grey: all failed markers ($\eta < 10^{23}$ Pa·s). Black: strongly failed markers ($\eta < 10^{22}$ Pa·s). Percentage numbers of all sedimentary markers. Insets: temporal evolution of the percentage of Lagrangian markers that exhibit a plastic strain between $\varepsilon_w^0 = 0.5$ and $\varepsilon_w^1 = 1.5$.

The evolution of wedges with the same amount of weakening ($\varphi_w = 20°$, $C_w = 0.2$ MPa) but with different shortening velocity V_x is illustrated with snapshots of the second invariant of the strain-rate tensor and accumulated plastic strain (Fig. 11) after an equal volume of incoming material, at 5.6 Ma for DS2 ($V_x = 1$ cm/a) and 1.13 Ma for DS3 ($V_x = 5$ cm/a). In general, both wedge halves evolve by in-sequence development of shear zones. Strain rates of the slow DS2 simulation indicate dominant shear band activity at the wedge front. In the wedge, slightly increased strain rates indicate frontward verging out-of-sequence shearing along previously active weakened zones (Fig. 11a). Accumulated plastic strain values indicate the weakening of frontward verging shear zones above the weak base. Plastic strain in conjugate backthrusts is below the critical value for initiation of their weakening (Fig. 11b). Imbricate thrust zones are flatter above the strong décollement than above the weak décollement part. Backthrusts cut earlier shear zones.

In model DS3, a larger number of high strain-rate shear zones than in model DS1 contribute to the wedge shortening (Fig. 11c). Frontward and backward verging shear zones are conjugate. Above the relatively weak base, shear zones in model DS3 are steeper and more closely spaced than in model DS2 (Fig. 11d). Shear zones above the strong décollement do not evolve in sequence. Out-of-sequence shear zones lead to imbrication of tectonic lenses between anastomosed shear zones (Fig. 11d).

Vertically averaged horizontal shear stresses are quantified within the wedge to test the effect of shortening velocity on the potential development of strike-slip shear zones above the décollement discontinuity (Fig. 12a and b). As the applied numerical code is based on a viscous Stokes flow, it is expected that stresses increase where the shortening velocity is boosted. However, the plastic rheological law sets an upper threshold to stresses. Although strike-slip shear zones cannot be identified within strain-rate plots (Fig. 11), vertically averaged horizontal
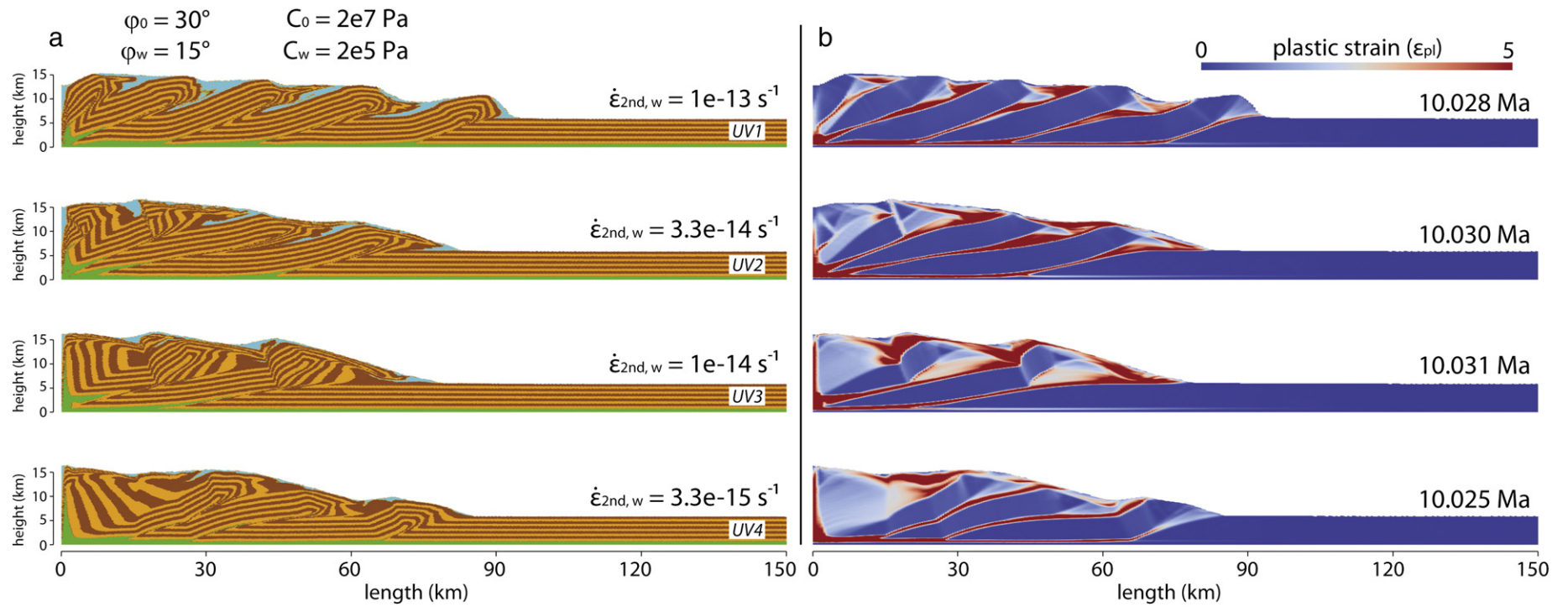
Fig. 6. Profiles at $y = 25$ km across velocity-weakened uniform simulations after 11.5–11.6 Ma with thresholds decreasing from top to bottom. a) Deformed sediments inferred from Lagrangian markers. Same colour code as Fig. (3). b) Accumulated plastic strain. Large strain areas in piggy-back style depressions portray gravity-driven mass flows.
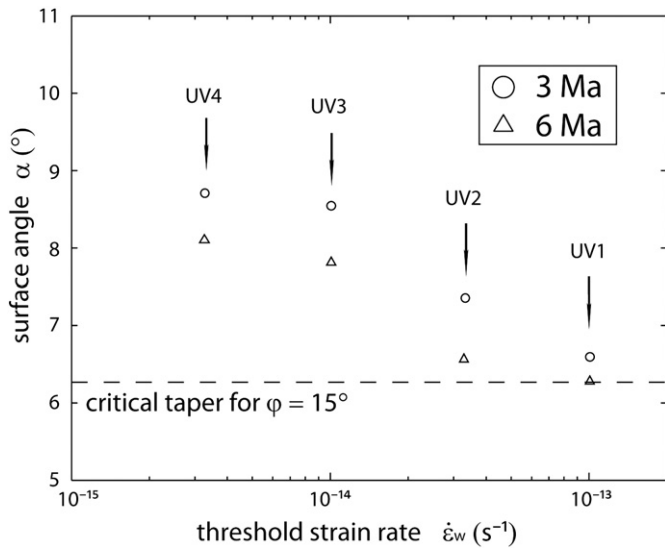
Fig. 7. Analytical test of numerical results of velocity-weakened uniform wedges. Dashed line: theoretically derived minimum critical taper for an internal friction angle of $\varphi = 15$. Circles: Surface slopes calculated by linear regression at $y = 25$ km after 3 Ma run time. Triangles: after 6 Ma run time.

shear stresses indicate their potential occurrence along the décollement strength change (Fig. 12a,b). Maximal values for averaged horizontal shear stresses in map view are ~70 MPa for both models, DS2 and DS3.

Surface slopes of the DS2 and DS3 simulations are analytically identical because the critical wedge theory is time independent. Plots of these surface angles at 5.6 (DS2) and 1.13 Ma (DS3) run time show that wedge tapers are steeper for faster shortening (Fig. 12c). Model

DS2 exhibits slopes ~1° steeper than the analytical prediction, with a smooth transition between the two model parts. Tapers of model DS3 are up to 5° steeper than the prediction above the strong décollement and around 3° steeper than the critical minimum in the area with a weak base (Fig. 12c). In general, all numerical wedge tapers are found to be within the stable area of the plot (Fig. 4a).

3.2.1.2. Sediment thickness H = 2.5 km. Rock with a brittle/plastic rheology gets stronger with depth, i.e. larger deviatoric stresses are needed to fail the material. The maximal strength of a pile of equal material is therefore at its bottom and depends on the dynamic pressure. Simulations with an initial "sediment" thickness of 2.5 km test this hypothesis (Fig. 13).

Accumulated plastic strain of models with $\varphi_w = 20°$ and $V_x = 2$ cm/a shows shear zones connected over the whole model width and curved where the switch in décollement strength is placed (Fig. 13a). The deformed wedge displays forward-verging imbrication above the weak and strong bases. Thrust faults have wider spacing above the weak décollement (Fig. 13a). A horizontal slice of the second invariant of the strain-rate tensor at $z = 1.5$ km shows that the most active frontal shear zones are interrupted and offset at the boundary between the different décollements (Fig. 13b). Along this offset, a relatively high strain-rate zone occurs.

Highly strained narrow shear bands reaching the wedge surface are more numerous than in the slower-compressed model (Fig. 13c). The deformation front above the weak base is shortened by several coeval shear zones. No frontal shear zone extends over the whole width of the model. Horizontal and vertical slices of strain rate show a large deformation zone without strain localization along the wedge front (Fig. 13d). Towards the rear of the wedge, active, i.e. high strain-rate shear zones are offset along the basal strength boundary, marked by a slight increase of strain rate.
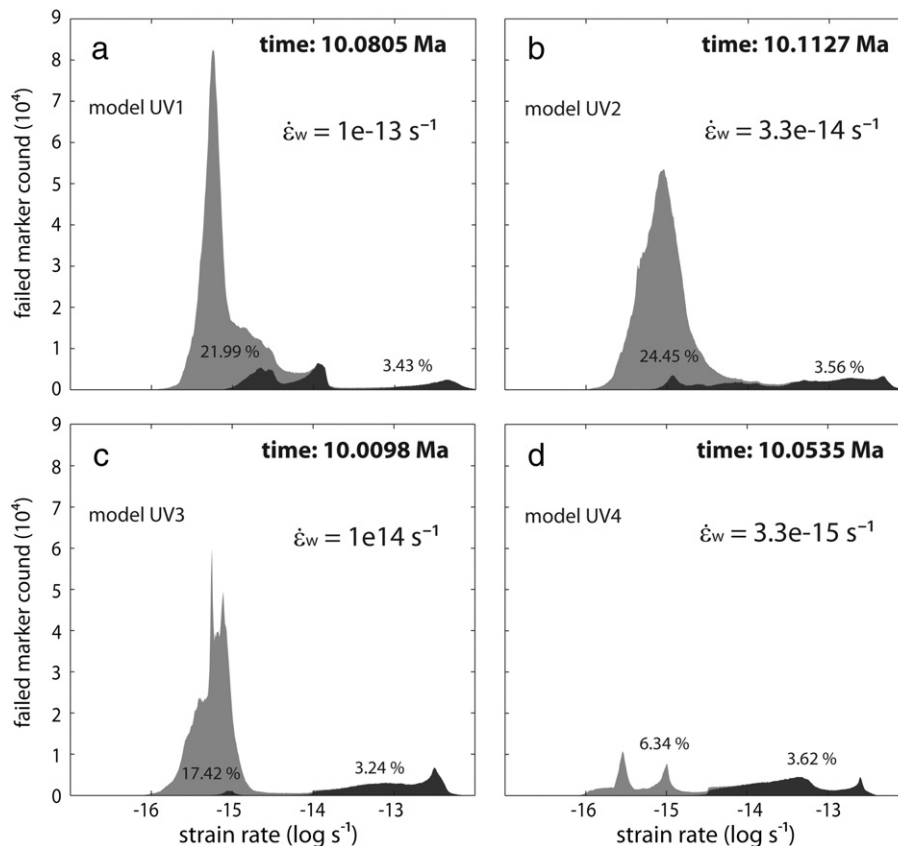

Fig. 8. Strain-rate distribution of plastically yielded Lagrangian markers within the wedge of simulations UV1–4 with different thresholds for velocity weakening after ~10 Ma run time. Grey: all failed markers ($\eta < 10^{23}$ Pa·s). Black: strongly failed markers ($\eta < 10^{22}$ Pa·s). Percentage numbers of sedimentary markers.
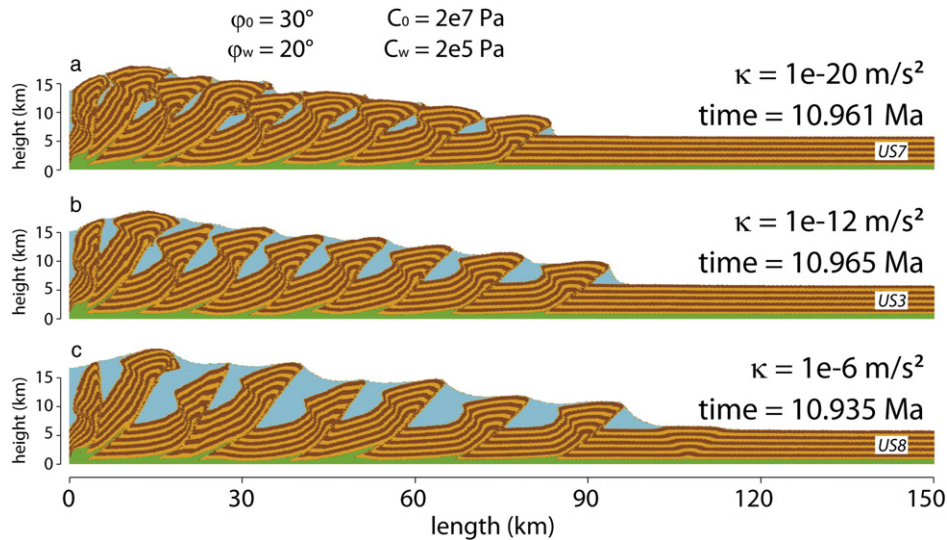
Fig. 9. Snapshots of wedges with identical amount of strain weakening ($\varphi_w = 20°$) and different surface diffusion constants κ after ~11 Ma run time. Same colour code as in Fig. (3).

3.2.2. Velocity-weakening models (DV models)

3.2.2.1. Sediment thickness H = 5 km.
Velocity-weakened simulations ($\dot{\varepsilon}_w = 3.3 \cdot 10^{-14}$ s^{-1}) with an initial sediment thickness $H = 5$ km show very different wedge evolutions according to bulk shortening velocity (Fig. 14). This contrasts with strain-weakened models, for which bulk shortening velocity has no major impact (Fig. 11). The wedge above the weak décollement of a slowly shortened model ($V_x = 1$ cm/a) is characterized by shallow-dipping ramps cut by steep backthrusts (Fig. 14a). A horizontal slice showing the second invariant of the strain-rate tensor at $z = 1.5$ km reveals a narrow shear zone along the boundary of décollement strength, separating a narrow, steep taper ($y = 0$–50 km) from a wide, flat one (Fig. 14b). Across the wedge, narrow, high strain-rate shear bands only occur at the wedge front; out-of-sequence deformation is absent.

The simulation with a shortening velocity of $V_x = 5$ cm/a exhibits frontward-verging shear zones with minor backthrusts (Fig. 14c). Both wedge parts exhibit steeper tapers than their counter parts of the $V_x = 1$ cm/a model. A consequence of the steep tapers is large finite strain representing gravity avalanches at the surface (Fig. 14c). The wedge is roughly equally narrow over the whole model width with no significant offset of the deformation front across the basal strength boundary (Fig. 14c). Nevertheless, a horizontal slice of the second invariant of the strain-rate tensor at $z = 1.5$ km shows a narrow high strain-rate shear zone along this boundary (Fig. 14d). Strain rates also illustrate that several active shear zones, not only the frontal ramp as in simulation DV1 (Fig. 14b), accommodate shortening of the wedge.

3.2.2.2. Sediment thickness H = 2.5 km.
In contrast to simulations with a cover thickness $H = 5$ km (Fig. 14), models with $H = 2.5$ km exhibit similar wedge lengths (x-axis) for different shortening velocities but at equal incoming volume (Fig. 15). The wedge of model DV3 shows mainly frontward verging shear zones above both, weak and strong bases (Fig. 15a). Sporadic backthrusts above the weak décollement are steep. Slices of the second invariant of the strain-rate tensor at $z = 1.5$ km and $y = 0$ indicate that the two frontal shear zones are active without noticeable out-of-sequence deformation (Fig. 15b). A narrow shear zone along the basal strength boundary offsets the wedge front at $y = 50$ km.

Increasing the shortening velocity to $V_x = 5$ cm/a leads to increased surface movement in form of gravitationally driven avalanches as described for models with a thicker sediment layer (Fig. 15c). The wedge above the weaker décollement exhibits more backthrusts than

in experiment at $V_x = 1$ cm/a. Shortening takes place along several shear zones in the wedge part with the relatively strong base (Fig. 15d).

4. Discussion

Modelling results demonstrate (i) that there are major differences in structural and dynamic evolution depending on the amount and style of material weakening and (ii) that strain and strain-rate dependent weakening of the friction angle has a strong influence on the structural evolution along strike-slip transfer zones.

4.1. Strain vs. velocity weakening

There are obvious mechanical differences between strain-weakening and velocity-weakening simulations. Strain-weakening routines decrease cohesion and/or friction angle when accumulated plastic strain reaches a previously defined threshold. Once the material weakens, it remains weak and deformation remains localized within the weak zones. On the other hand, velocity weakening occurs when a threshold strain rate is exceeded. This is transient since the material recovers its initial strength as soon as the strain rate falls below the weakening threshold. This can be compared to healing of previously active shear zones. Healing and strength recovery of active fault zones are natural processes (Bos and Spiers, 2000; Bos et al., 2000) already investigated in numerical modelling (Gerya, 2013; Tackley, 2000). Nevertheless, these previous numerical studies applied a strain-weakening routine to initiate the loss of strength but a healing strain- and/or temperature-rate. An important difference of this strain-weakening/healing approach and velocity weakening of this study is that initial weakening is instantaneous in velocity-weakened systems, but needs some amount of plastic deformation if weakening is strain-dependent.

The differences in dynamical and structural evolution of strain- and velocity-weakened systems are demonstrated by displaying the weakened zones during the development of a strain-weakened and a velocity-weakened simulation (Fig. 16). The strain-weakened simulation exhibits several weak bands, which all define an active, previously active or reactivated shear zone (Fig. 16a). Shear bands initially occurred in conjugate sets. With ongoing shortening, frontward-verging shear zones were preferred and backthrusts more or less abandoned (see also Fig. 3a). Strain weakening favours the out-of-sequence reactivation of previously weakened shear zones. The stronger the weakening effect, i.e. the lower φ_w, the narrower the shear zones (Fig. 5). With further growth of the wedge, shear zones close to the rear passively
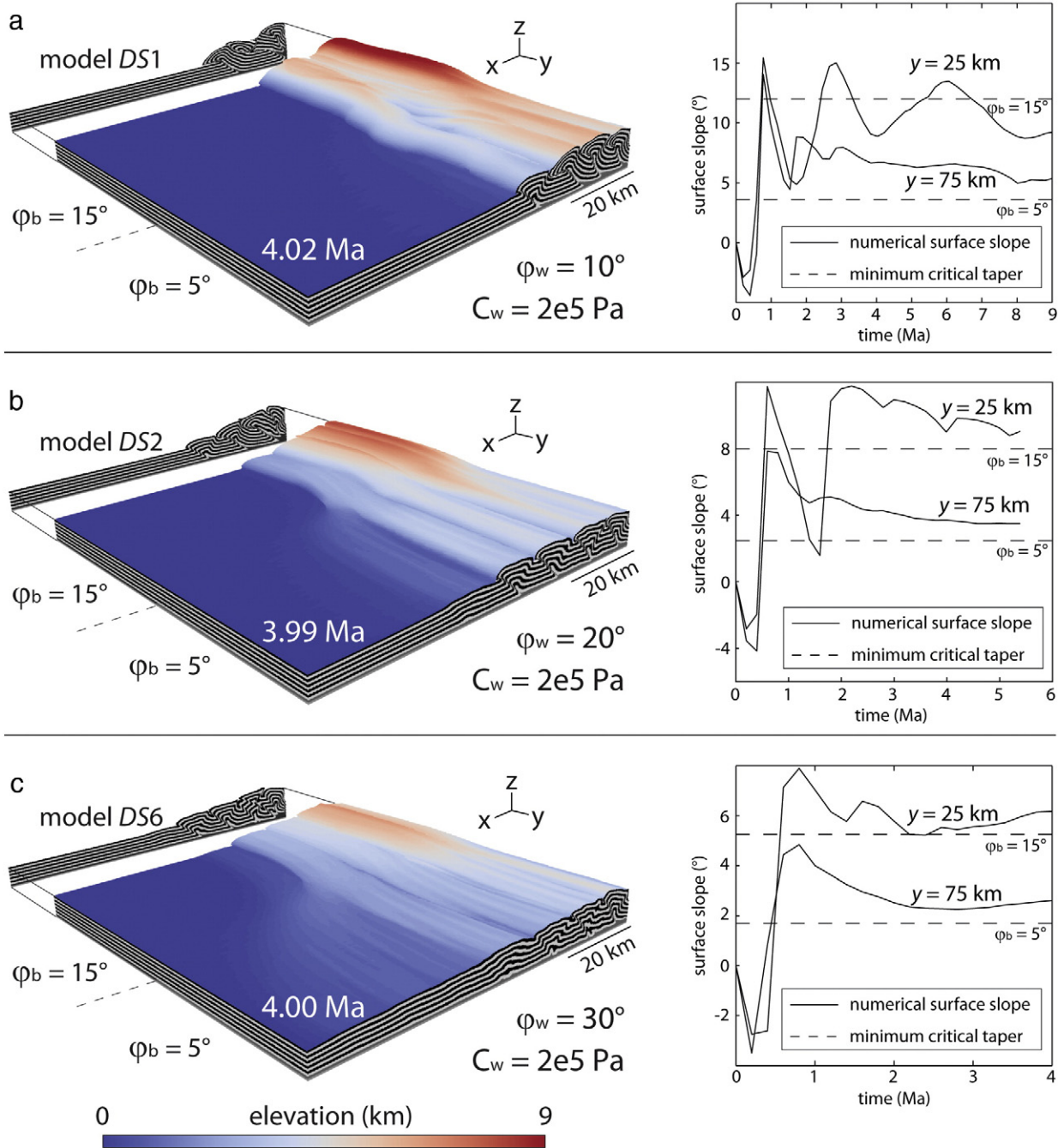
Fig. 10. Topography of dual simulations with change in décollement strength φ_b after ~4 Ma run time for different values for weakening (φ_w). Black/white: deformed strata at $y = 0$ and $y = 100$ km. Right column: temporal evolution of surface slopes at $y = 25$ and $y = 75$ km width for each model (solid lines). Dashed lines: theoretical critical minimum tapers depending on internal and décollement strength.

rotate towards steeper attitudes, although the critical wedge theory predicts shallower dipping shear planes according to main stress orientations (Fig. 16a). Single shear zones within strain-weakened models accommodate more displacement if weakening is increased. The spatial and temporal development of shear zones is also strongly dependent on the amount of weakening (φ_w, C_w). These results support earlier studies investigating the effect of strain weakening on thrust wedges (Ellis et al., 2004; Selzer et al., 2007).

In velocity-weakened simulations, only the instantaneously active shear zone is weak (Fig. 16b). Single shear zones are constantly active for ~4 Ma. Low-inclination shear zones evolve into ramp to flat systems towards the wedge toe (Fig. 16b; 7.46 Ma). The décollement is active in front of the active shear zone (increased strain rates at 7.46 Ma). This

indicates pure shear shortening and an increase of viscous stresses within underthrusting sediments (7.46 Ma). Further shortening in front of the active shear zone ends with a jump forward of the active shear zone (Fig. 16b; 9.37 Ma). The new ramp develops at the wedge toe, which is defined by a surface flow deposit. Spacing between shear zones is therefore mainly defined by the extension of gravity-driven flows. Down-slope, gravity-driven mass flows lower the taper at the wedge toe (9.37 Ma). Generally, higher local strain rates are reached within shear zones than in strain-weakened models (Fig. 5 and 8). Nevertheless, the main part of failed material is characterized by rather low strain rates, around 10^{-15} s^{-1} (Fig. 8a–c).

For rate-dependent weakening models, recurrence of the above described events (pure shear and stress increase, ramp development,
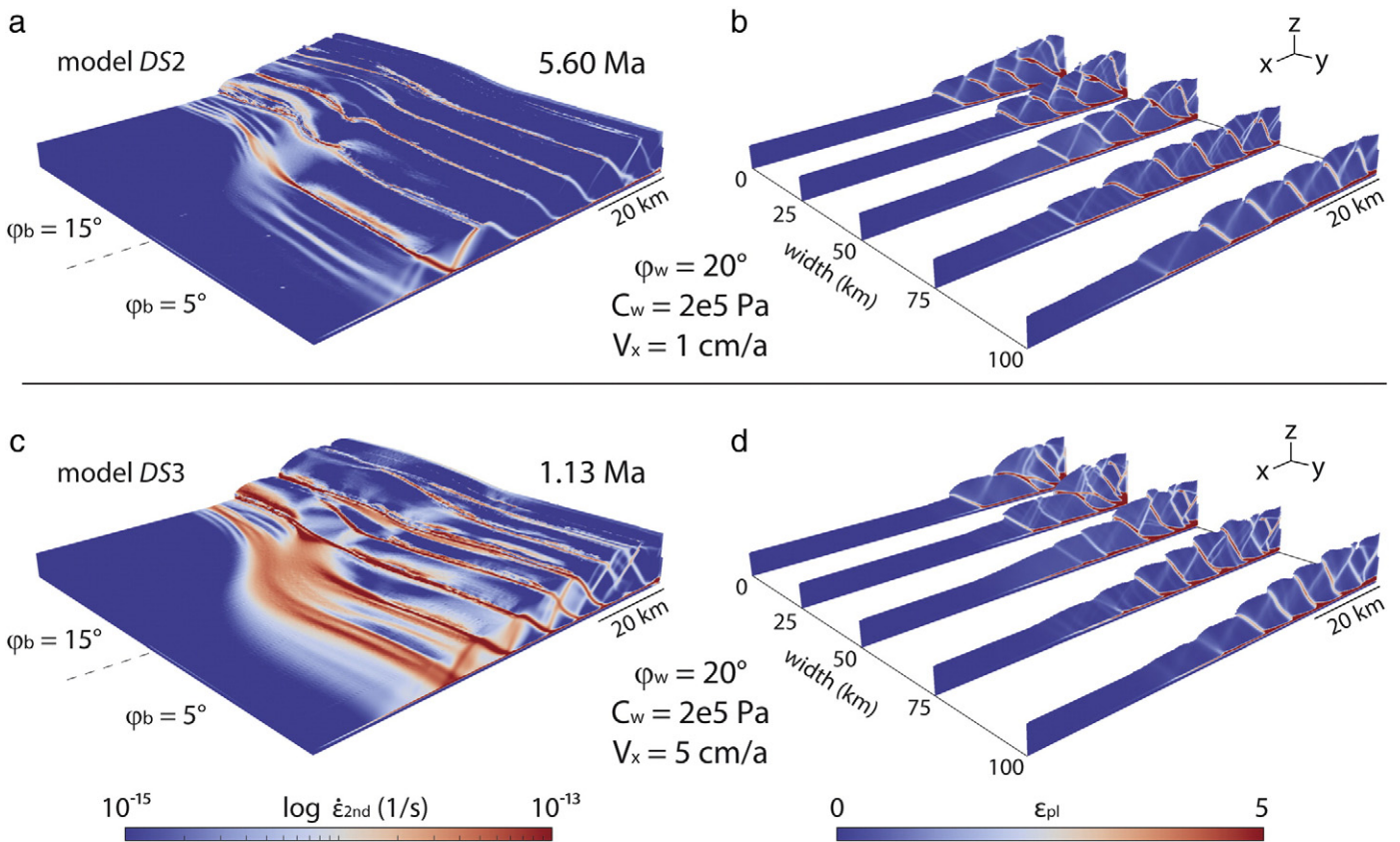
Fig. 11. Effect of shortening velocity after ~56 km of incoming sediment. a) Strain rate and b) slices of accumulated plastic strain of a slow compressed wedge with $V_x = 1$ cm/a. c) Strain rate and d) slices of accumulated plastic strain of a fast compressed wedge with $V_x = 5$ cm/a.

gravity flow) leads to an in-sequence imbrication typical of fold-and-thrust belts. Mass flows at the wedge toe occur only in velocity-weakened setups (Fig. 16) because the response of the material strength is instantaneous, whereas it needs building up some minimal amount of plastic strain in strain-weakened material.

4.2. Comparison with the critical wedge theory

The critical wedge theory predicts a minimum and a maximum critical total taper (surface α + base β angles), depending on the internal strength of the wedge material, the strength of the décollement and the base angle β (Dahlen, 1984; Dahlen et al., 1984; Davis et al., 1983).

Furthermore, inclination of the main stress can be analytically predicted and be compared to numerical wedge models (Ruh et al., 2012, 2013).

Strain weakening leads to a non-recoverable reduction of the internal friction angle and cohesion. Surface slopes of uniform, strain-weakened simulations (US models) indicate that the strength of the wedge is defined by its weakened strength (φ_w, C_w). The more the wedge is weakened, the steeper the surface slopes (Figs. 3a and 4b).

Surface slopes of velocity-weakened simulations ($\varphi_w = 15°$) are steeper than the analytical prediction made with an internal friction angle of $\varphi = 15°$ (Fig. 7). In contrast to strain-weakened models, the internal strength is not defined by the weak friction angle and cohesion because weakening takes place only within one shear zone that heals to the initial strength when the strain rate decreases. Steeper tapers
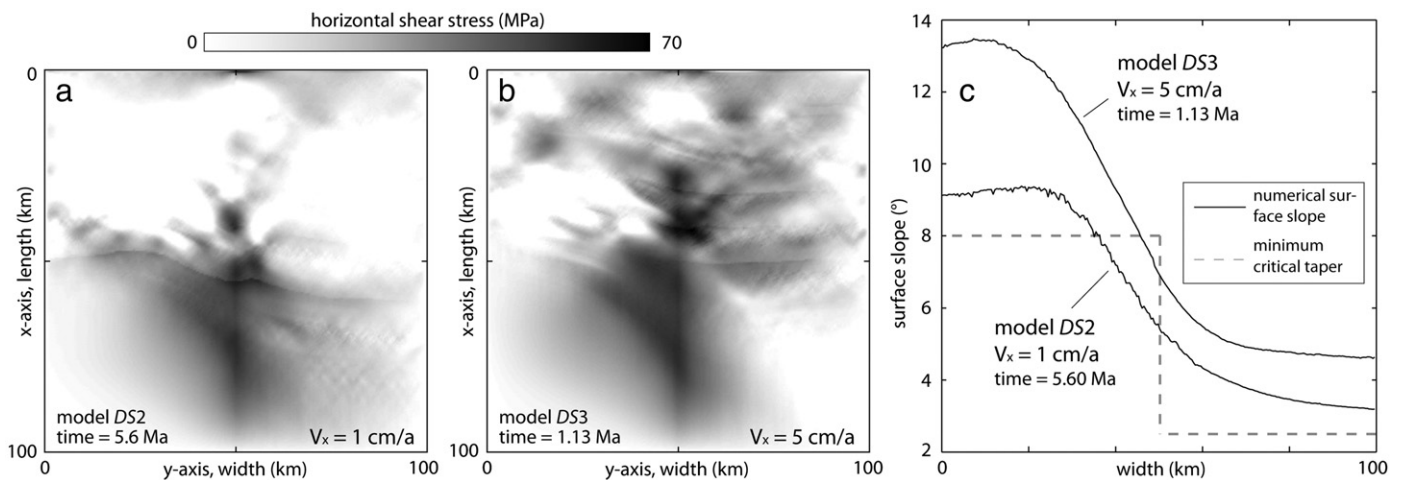

Fig. 12. Vertically averaged horizontal shear stresses within the wedge of simulations with a) $V_x = 1$ cm/a and b) $V_x = 5$ cm/a. c) Solid lines: numerically derived surface slopes over width (y-axis) for slow and fast compressed wedges. Grey dashed line: analytical critical minimum taper.
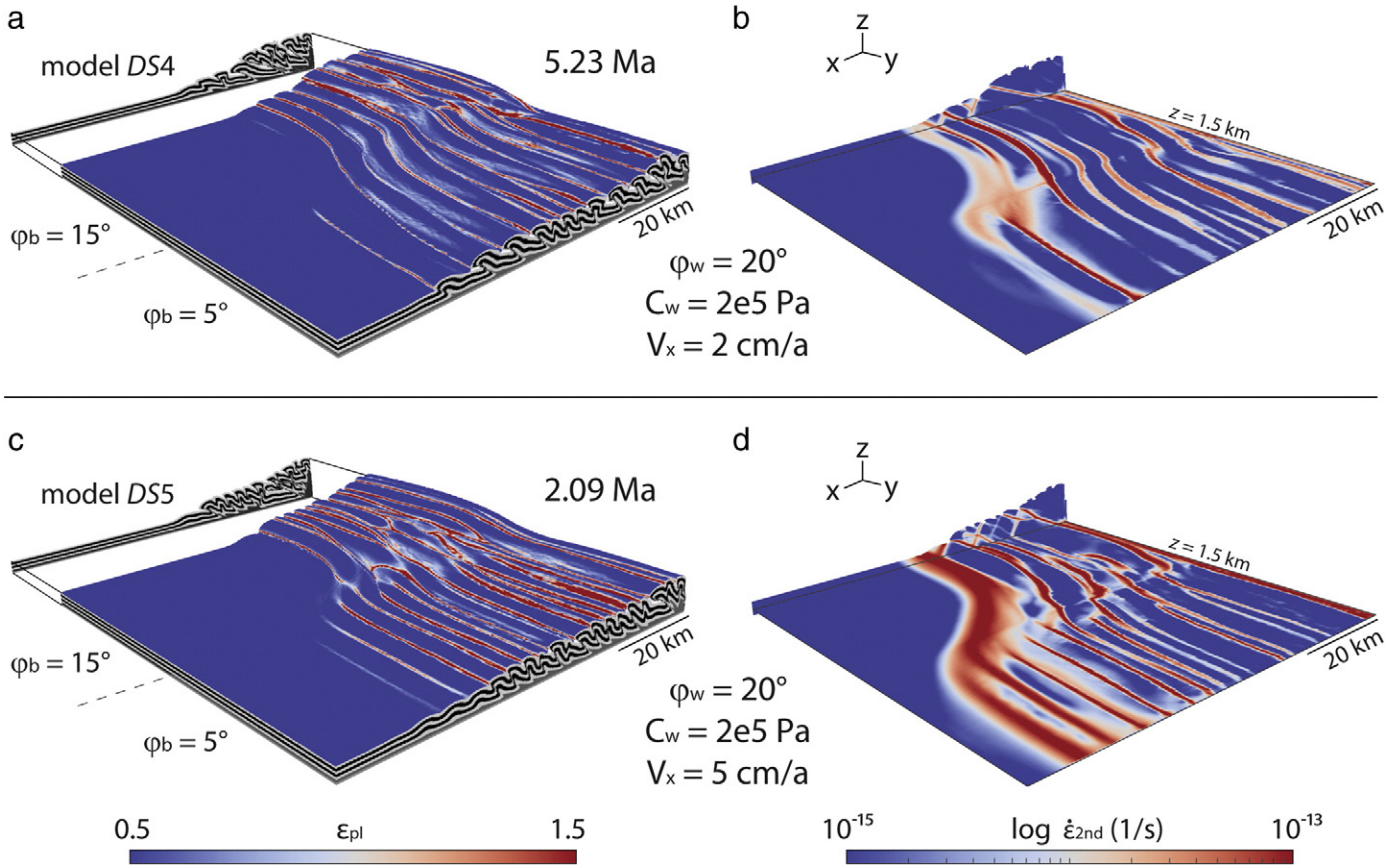
Fig. 13. Strain-weakened simulations with lateral décollement strength change and a sediment thickness of $H = 2.5$ km with different shortening velocities V_x. Left column: accumulated strain with profiles of deformed strata (black/white) at $y = 0$ and $y = 100$ km. Right column: slices of the second invariant of the strain-rate tensor at $z = 1.5$ km (horizontal slice) and $y = 0$ (vertical slice).

for lower threshold is understandable because weakening occurs at lower strain rates, i.e. earlier, and weakens more intensely shear zones within the wedge. A weaker internal strength results in steeper tapers. However, due to the time-independency of the critical wedge theory, comparison with velocity-weakened simulations is inadequate.

Surface slopes in both parts of dual models are, like in uniform models, steeper where weakening is more efficient (Fig. 10). According to the critical wedge theory, normal faulting takes place when surface slopes exceed the maximum critical taper. In the strong décollement part of model DS1, the minimum and maximum critical tapers are identical, because the internal strength $\varphi_w = 10°$ of the wedge is weaker than the underlying décollement $\varphi_b = 15°$. This explains alternating thrusting and normal faulting (Fig. 10a). Surface slope oscillations result from these normal faults, which instantly lower the taper. Surface slopes of simulations with wedges weakened to $\varphi_w = 20°$ and $30°$ do not develop normal faulting and are consequently slightly above their critical minimum in both wedge parts (Fig. 10b,c).

Although the analytical theory is time-independent, the bulk shortening velocity has a strong effect on average surface slopes (Fig. 12c). Model DS3 with $V_x = 5$ cm/a has a surface slope 2–4° steeper than model DS2 with $V_x = 1$ cm/a. The reason lies in the numerical treatment of plasticity. If plastic failure occurs, viscosity is decreased so that maximal stresses are at the local yield stress (see Appendix A). Practically, this means that the active décollement is a layer with a low viscosity. This low viscosity base develops shear stresses depending on the velocity difference through the layer ΔV, its viscosity η and its thickness H_b:

$$\tau_b = \eta \frac{\Delta V}{H_b} \tag{2}$$

It is obvious that the faster the bulk shortening velocity, i.e. the potential shear velocity within the décollement, the larger the basal shear stresses. Viscous shear stresses within the basal décollement drag the "sediments" towards the rear and increase the taper. The surface slope gains ~1° for a 500 m thick décollement with a viscosity of 10^{19} Pa·s and a shortening velocity of $V_x = 1$ cm/a (Davis and Engelder, 1985; Ruh et al., 2012). This angle value matches the excess of surface slope in model DS2 with respect to its critical minimum taper (Fig. 12c). An increase of bulk shortening velocity to $V_x = 5$ cm/a increases basal shear stresses and additional surface slope by a factor of 5. The excess of taper is lower than 5°, because the décollement has a lower effective viscosity than in the slow model. Surface slopes of model DS3 fit the values predicted by the critical wedge theory combined with basal décollement drag (Fig. 12c).

4.3. Effects of plastic/brittle weakening on dual models

Different amounts and types of weakening influence the evolution of uniform numerical wedges. Therefore, input parameters such as bulk shortening velocity, amount and type of weakening and sediment initial thickness affect the structural and dynamic developments of wedges where the décollement strength changes.

The influence of shortening velocity on dual, strain-weakened models is minor. Although fast wedges undergo larger strain rates than slow ones (Fig. 11a, c), the horizontal shear stresses acting along the boundary of décollement strength are similar for simulations that started with a 5 km thick sedimentary layer (Fig. 12a, b). Results of models with an initial 2.5 km thick sedimentary layer reveal that an increased amount of weakening can lead to localization of a high strain rate, vertical shear band along the décollement strength-boundary (Fig. 13b, d). Plots of plastic strain show that the transfer zone between
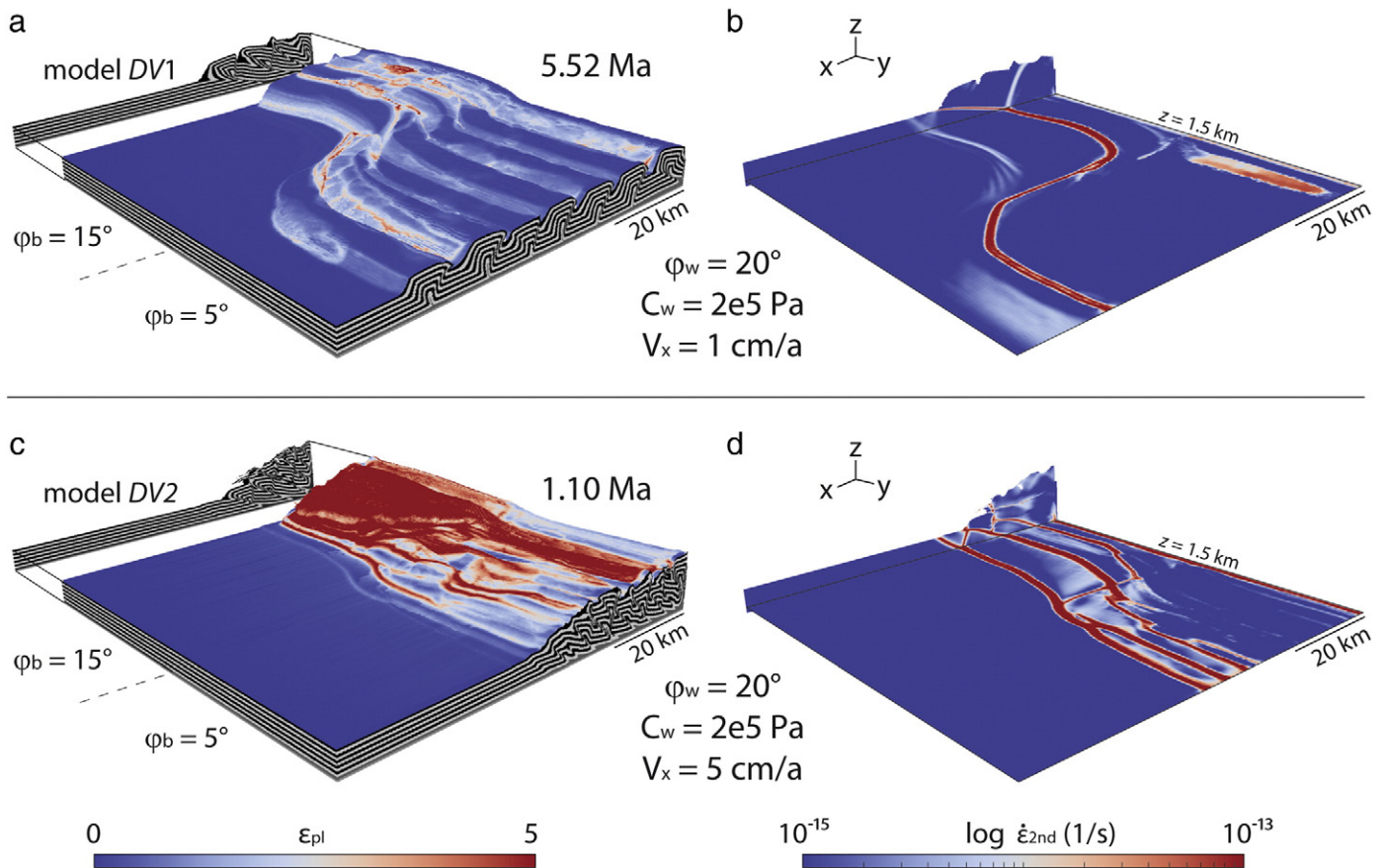
Fig. 14. Velocity-weakened simulations with lateral décollement strength change and an initial sediment thickness of $H = 5$ km shortened at 1 cm/a (model *DV*1) and 5 cm/a (model *DV*2). Left column: accumulated strain with profiles of deformed strata (black/white) at $y = 0$ and $y = 100$ km. Right column: slices of the second invariant of the strain-rate tensor at $z = 1.5$ km (horizontal slice) and $y = 0$ (vertical slice).

a wide and a narrow wedge (above weaker/stronger décollements, respectively) is wider for less weakened simulations (Fig. 13a, c). Strike-slip movements in a thinner sediment layer are due to lower brittle/plastic yield strength than in thicker models. Therefore, smaller horizontal shear stresses are needed to yield the material.

Velocity-weakened numerical wedges exhibit major differences in deformational patterns and dynamic evolution. High strain-rate shear zones in the brittle/plastic wedge parallel to the décollement strength boundary develop independently of sediment thickness and bulk shortening velocity (Figs. 13, 14 and 15). Horizontal slices of velocities in *x*-direction and vertical profiles of strain rates of models *DS*4, *DV*1 and *DV*4 show that these shear bands are not cutting through the whole sediment package in strain weakened simulations (Fig. 17a). If sediments are velocity-weakened, sub-vertical strike-slip shear zones develop (Fig. 17b,c).

Like in uniform, velocity-weakened models, shallow-dipping normal shear zones act as detachments for surface mass flows. In dual simulations, mass flows occur at the toe of the wedge and all over the wedge surface above the relatively strong décollements (Fig. 18a). Such gravity-driven mass flows can be compared to mass waste events described in accretionary wedges, such as the Makran or the Gibraltar arc (Burg et al., 2008; Medialdea et al., 2004). In such accretionary complexes, fluid pressures are close to lithostatic pressures (Davis et al., 1983). Therefore, stable areas of wedges according to the critical wedge theory are narrow. A slight steepening of the surface slope results in normal faulting at the rear of a wedge to lower the taper. The numerical mass flows are initiated when surface slopes are close to the maximum critical taper (calculated with weakened internal strength) and are then constantly lowering the wedge taper although

the wedge is theoretically within the stable area, according to the critical wedge theory (Fig. 18b). An instantaneously weakened high strain-rate shear band suddenly changes the strength properties of the wedge area above the strong décollement and leads to a gravitational instability. The surface flow reaches the wedge toe, where the velocity discrepancy between flow and the underlying cover sequence is up to 7 cm/a.

4.4. Effects of cover sequence thickness and shortening velocity

Surface tapers of purely frictional wedges are, according to the critical wedge theory, independent of the cover sequence thickness. However, the yield strength of the cover sequence and the basal décollement both depend on this cover thickness. The shortening velocity should not influence the analytically derived surface slope because of the time-independency of the critical wedge theory. Nevertheless, more rapidly shortened ($V_x = 5$ cm/a) strain-weakened simulations yield slightly steeper tapers than if shortening velocity is $V_x = 1$ cm/a (Fig. 12c). This is due to the viscous formulation of the numerical code, which is therefore not purely frictional. The low viscosity of the failed décollement layer develops an additional basal drag towards the rear, according to Eq. (2). A faster shortening rate generates a stronger drag and therefore leads to a steeper surface taper than for slowly shortened wedges.

Theoretically, the shortening rate and the thickness of the cover sequence both strongly influence the development of sub-vertical strike-slip shear zones. Faster total shortening rates result in faster propagation of the wedge front and, in dual models, to faster offset between the two model parts. Faster offset development leads to higher
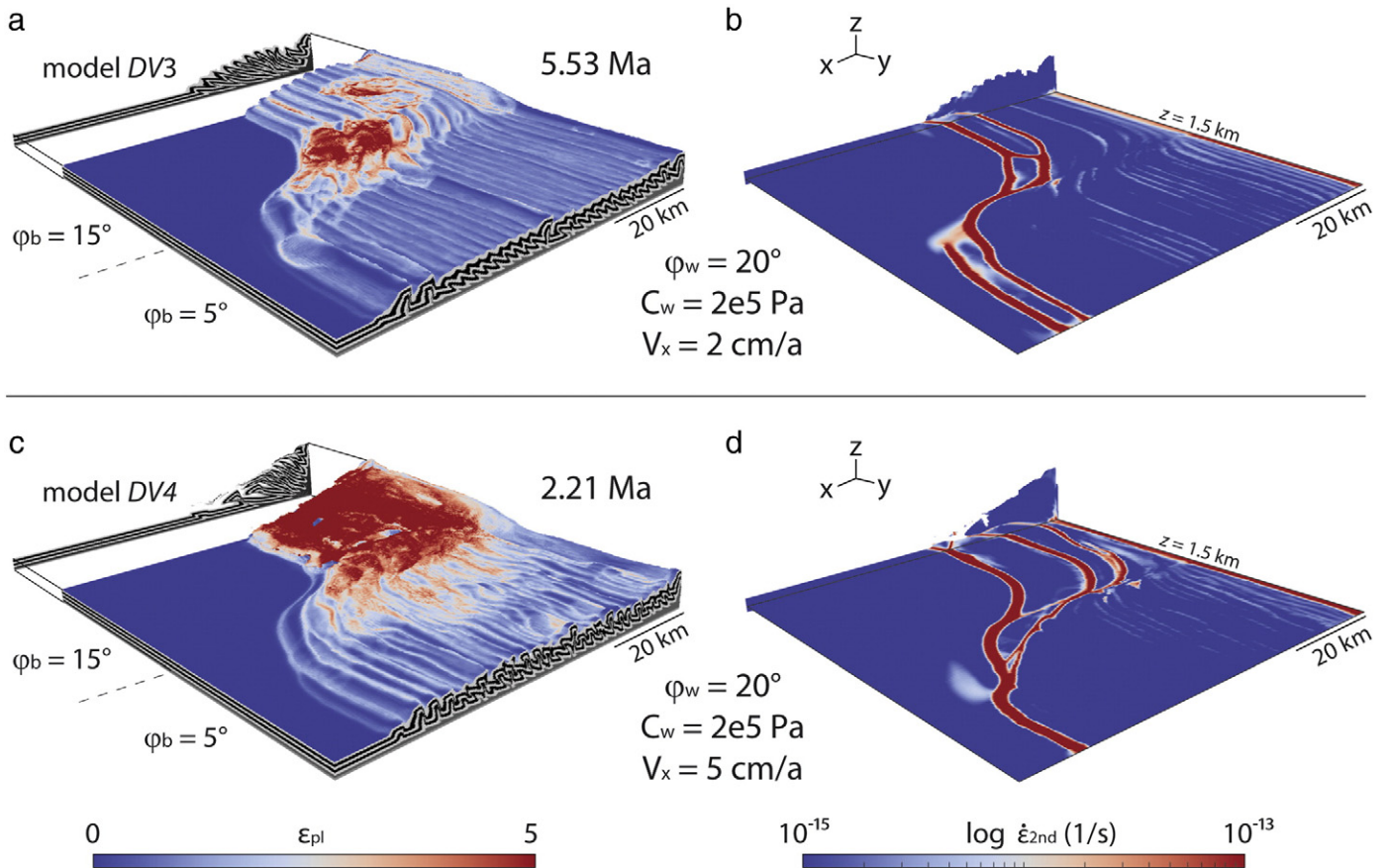
Fig. 15. Velocity-weakened simulations with lateral décollement strength change and a starting sediment thickness $H = 2.5$ km shortened at 2 cm/a (model *DV3*) and 5 cm/a (model *DV4*). Left column: accumulated strain with profiles of deformed strata (black/white) at $y = 0$ and $y = 100$ km. Right column: slices of the second invariant of the strain-rate tensor at $z = 1.5$ km (horizontal slice) and $y = 0$ (vertical slice).

horizontal shear stresses along the prescribed transition zone and therefore to a higher potential for the occurrence of strike-slip shear zones. Strain-weakened simulations do not exhibit strike-slip components along the transition zone, neither in slow nor in fast shortened models (Fig. 11) and maximal vertically averaged horizontal shear stresses are similar (Fig. 12a,b). Velocity-weakened simulations show shortening parallel strike-slip shear zones independent of shortening rate (Fig. 14). Faster shortened models ($V_x = 5$ cm/a) display several active thrust ramps to account for the shortening and wedges in both parts are steeper than in slowly shortened models (Fig. 14).

A thinner sedimentary cover has a lower yield strength at its base. Therefore, lower horizontal shear stresses are needed for yielding. In contrast to strain-weakened simulations with a cover thickness of $H = 5$ km, strain-rate slices of models with a 2.5 km thick cover indicate the potential development of narrow shear bands along the basal strength transition (Fig. 13). Like velocity-weakened simulations with a 5 km thick cover, strike-slip shear zones develop effectively in velocity-weakened simulations with a 2.5 km thick cover sequence (Fig. 15). Surface mass flows are restricted to velocity-weakened models and occur chiefly if shortening rate is faster than 1 cm/a.

4.5. Comparison to analogue models and natural systems

There are major differences in structural evolution numerical wedges depending on the style of weakening applied. Strain-weakened simulations produce shorter wavelengths of thrust sheets, steeper thrust ramps and more contemporaneously active shear zones than in velocity-weakened models. Strain-weakened simulations with weakened internal friction angles of $\varphi_b = 10–20°$ (Fig. 3) are in terms of structural development comparable to the offshore Makran (Fig. 7 in Grando and McClay, 2007). There, uprising fluids are sourced at the

basal décollement level of the active imbricate fan with a piggy-back style. Velocity-weakened simulations exhibit thrust ramps that flatten towards the wedge toe, where thrust sheets overthrust the underlying undeformed sequence along close to horizontal shear zones (Fig. 6). Such ramp/flat systems are observed in several seismically active fold-and-thrust belts like across the Los Angeles area (Davis et al., 1989), Western Taiwan (Yue et al., 2005) and the Appalachians (Fig. 2 in Suppe, 1983).

Cotton and Koyi (2000) and Nilforoushan and Koyi (2007) investigated structures that develop along a sudden change from ductile to frictional décollement. Cotton and Koyi (2000) produced strike-slip faults parallel to the shortening direction but the contrast of basal strength in their setup is large. Models of Nilforoushan and Koyi (2007) do not exhibit clear strike-slip faulting. The deformation front along the basal strength transition is curved. Calassou et al. (1993) set up a milder change in basal strength, with both parts of the base defined by a frictional rheology. The resulting transfer zone also developed as bending of wedge frontal structures without strike-slip faults.

Like in experiment 3 of Calassou et al. (1993) and experiments of Nilforoushan and Koyi (2007), strain-weakened numerical wedges of this study form curved frontal structures instead of strike-slip faults (Figs. 11, 13 and 17a). This agrees with the fact that strength of layered sandbox models is also strain-dependent (Graveleau et al., 2012; and references therein).

In nature, large-scale strike-slip fault systems parallel to the shortening direction in fold-and-thrust belts are often induced by basement structures, such as the Minab–Zendan transfer fault between the Zagros fold belt and the Makran accretionary wedge (e.g., Regard et al., 2005), and strike-slip faults in central Zagros (Baker et al., 1993) and the Oregon accretionary prism (Tobin et al., 1993). Major sinistral strike-slip/tear faults exist in the Jura foreland fold-and-thrust belt (e.g., Mosar,
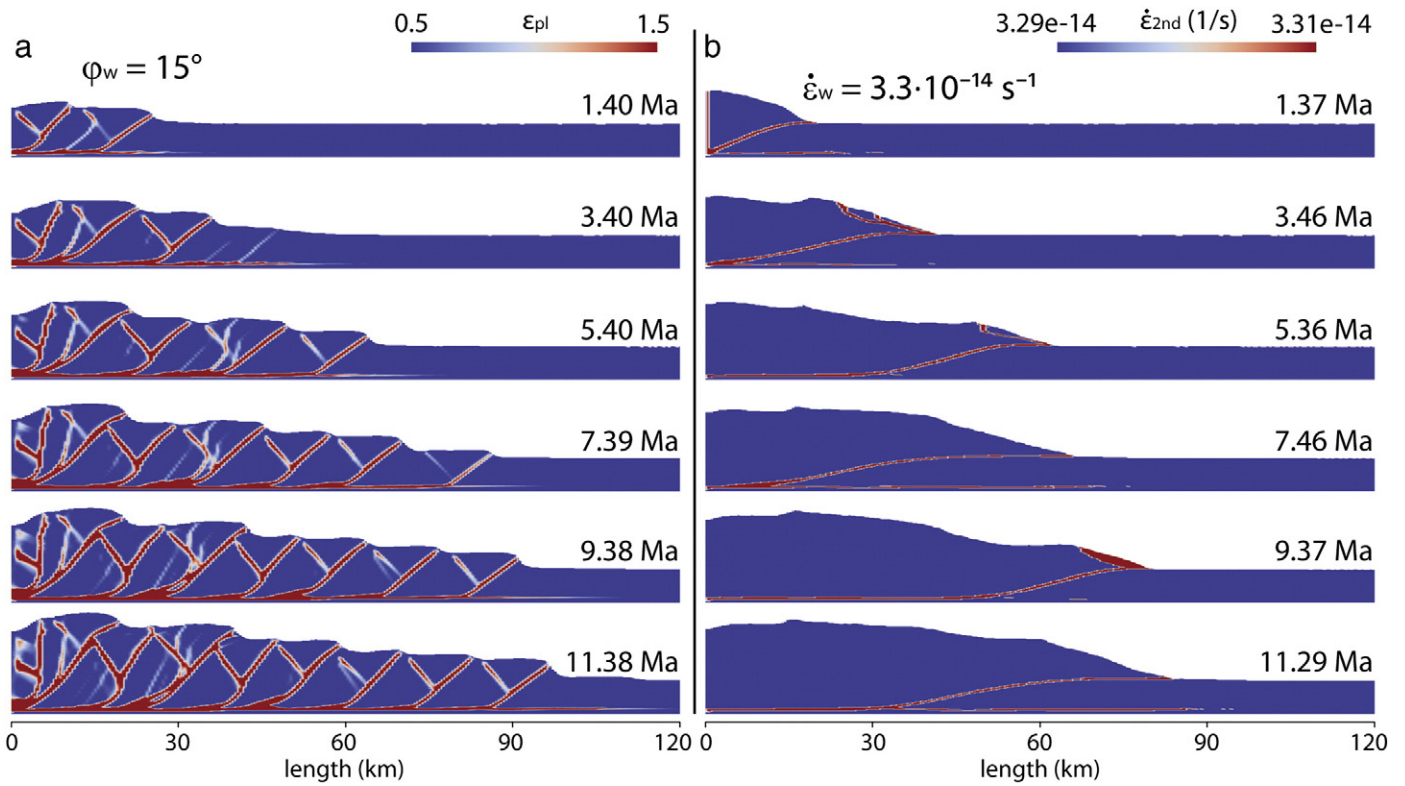
Fig. 16. Temporal evolution of weakened zones in strain- and velocity-weakened simulations. a) Accumulated plastic strain between ε_w^0 and ε_w^1 show weakened areas in a simulation with $\varphi_w = 15°$. b) Second invariant of the strain-rate tensor between $3.29 \cdot 10^{-14}$ and $3.31 \cdot 10^{-14}$ s^{-1} show weakened zones of a velocity weakened simulation with a weakening threshold of $\dot{\varepsilon}_w = 3.3 \cdot 10^{-14}$ s^{-1}.

1999; Sommaruga, 1999). These faults are almost transverse to the fold trend and do not affect the basement. According to simulations presented in this study, sub-vertical strike-slip zones limited to the sedimentary cover develop if wedges are velocity-weakened. Changes in thickness of the viscous salt décollement in the Jura mountains potentially lead to variations in basal strength, which can trigger strike slip faults.

5. Conclusion

New numerical models were performed to investigate the effects of strain vs. velocity weakening on the dynamics and structural evolution of uniform wedges and wedges with a lateral change in décollement strength. Uniform settings, i.e. simulations without any along-strike rheological variation, show that:

1. Strain weakening generates shear zones that remain active throughout shortening. Increased weakening causes stronger localization into fewer shear zones with larger offsets. Out-of-sequence shear zones tend to become steeper with increasing distance to the wedge toe.

2. Numerical surface slopes compared to those from the analytical critical wedge theory show that the internal strength of strain-weakened wedges depends on weakened strength C_w and φ_w. A wedge is as strong as its weakest shear zone.

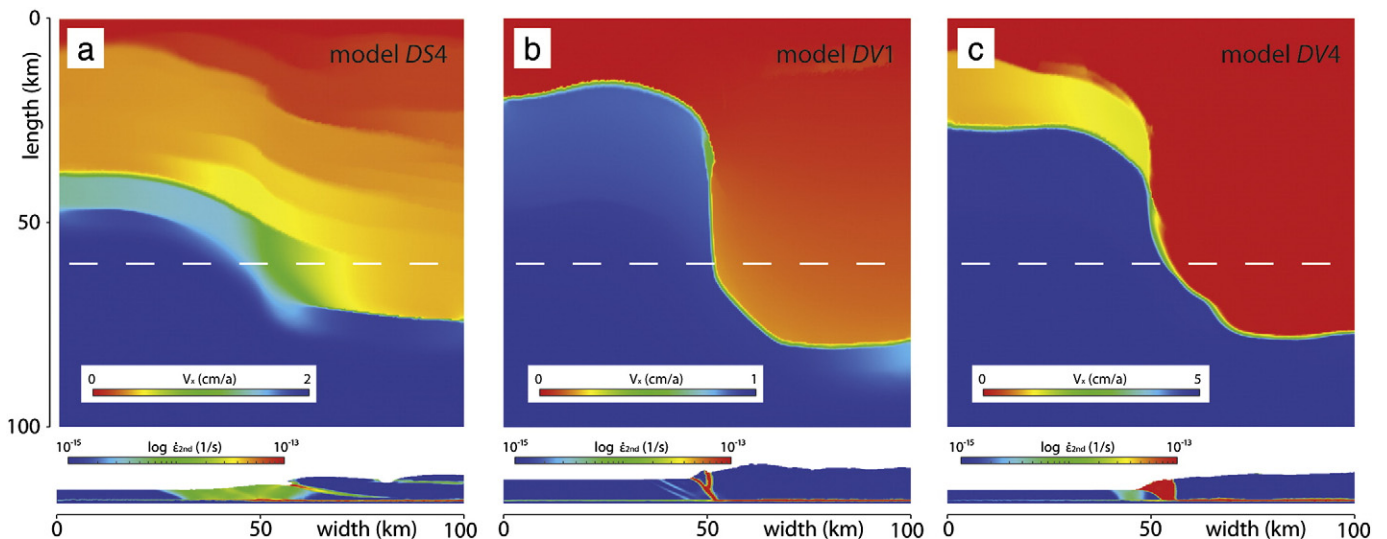**Fig. 17.** Horizontal slices at $z = 1.5$ km illustrating velocities in x-direction and related vertical profiles of the second invariant of the strain-rate tensor at $x = 60$ km for models DS1 (a), DV1 (b) and DV4 (c).
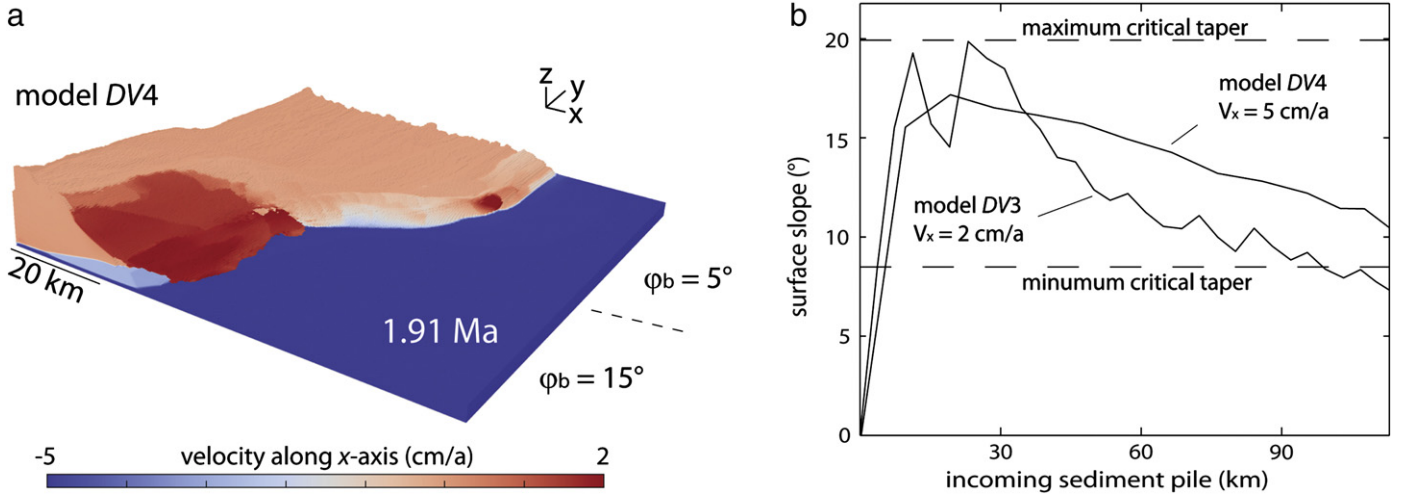
Fig. 18. a) Surface mass flow inferred by numerical velocity of a velocity weakened simulation *DV*4 (see Table 3) after a run time of 1.91 Ma. Velocities below zero move towards the backstop, velocities above zero move away from the backstop, towards the wedge toe. b) Evolution of surface slope at $y = 25$ km of simulations *DV*3 and *DV*4. Maximum critical tapers of simulations *DV*3 and 4 are, depending on the effect of weakening, 20–29°.

3. Velocity-weakened wedges develop low-angle ramping shear zones and gravity-driven mass flows at the toes, which are triggered by the instantaneous response of internal strength to locally increased strain rate.
4. Lower strain-rate thresholds for velocity weakening produce steeper surface slopes, like in strain-weakened simulations.

The most important results from dual simulations with a change in frictional décollement strength are:

1. The bulk shortening velocity is not a critical factor to build up lateral shear stresses in strain-weakened models but strongly influences the evolution of velocity-weakened models.
2. Rather steep normal shear zones occur in strain-weakened wedges if the internal friction angle is reduced to a value lower than the décollement friction angle. In velocity-weakened simulations, normal shear zones trigger large mass flows and constantly lower the surface taper.
3. Strain-weakened dual simulations develop a curved frontal thrust linking the weak to the strong décollement part.
4. Basement independent tear faults in the Jura mountains are not reproducible with strain-weakened wedge models. Velocity weakening is necessary to develop sub-vertical narrow shear zones with a strike-slip component.

Acknowledgements

Appendix A. Numerical formulation

A.1. Governing equations

The mechanical model is built on the equations for conservation of mass assuming incompressibility (i.e., sediment compaction is neglected)

$$\frac{\partial u_i}{\partial x_i} = 0 \tag{A1}$$

and the conservation of momentum, the Stokes equation

$$-\frac{\partial P}{\partial x_i} + \frac{\partial \tau_{ij}}{\partial x_j} = \rho g_i \tag{A2}$$

where

$$\tau_{ij} = 2\eta \dot{\varepsilon}_{ij} \tag{A3}$$

and

$$\dot{\varepsilon}_{ij} = \frac{1}{2}\left(\frac{\partial u_i}{\partial x_j} + \frac{\partial u_j}{\partial x_i}\right). \tag{A4}$$

P is dynamic pressure, i.e. mean stress, u_i the velocity ($u_1 = u_x$, $u_2 = u_y$, $u_3 = u_z$,), x_i the spatial coordinates ($x_1 = x$, $x_2 = y$, $x_3 = z$), τ_{ij} the deviatoric stress tensor, ρ the density, g_i the gravitational acceleration ($g_1 = g_2 = 0$, $g_3 = 9.81$ m/s^2), η the viscosity and $\dot{\varepsilon}_{ij}$ the strain-rate tensor.

If differential stresses exceed the yield stress, plastic failure follows the Drucker–Prager yield criterion with the plastic yield function F (Eq. (A5)) depending on the second invariant of the stress tensor τ^{II} and the yield stress σ_y

$$F = \tau^{II} - \sigma_y \tag{A5}$$

where

$$\tau^{II} = \sqrt{\frac{1}{2}\tau_{ij}^2} \tag{A6}$$

and

$$\sigma_y = P \cdot \sin\varphi + C \cdot \cos\varphi \tag{A7}$$

C is cohesion and φ the friction angle of the material.

A.2. Numerical implementation

The governing equations given in Appendix A.1 are solved numerically by discretising Eq. (A3) in an implicit manner, using an efficient OpenMP-parallelized multigrid solver, fully parallel on 16 (series *C*) or 32 (series *L*) threads. We adopted a standard geodynamic modelling approach, using an effective viscosity formulation for the numerical treatment of visco-brittle/plastic deformation (e.g., Buiter et al., 2006; and reference therein). Like for non-Newtonian (e.g. power-law) viscous rheology, effective viscosity for visco-brittle/plastic flows characterises a local ratio between the deviatoric stress and the strain rate (Eq. (A3)). At places where the plastic yielding condition is not

reached, deformation is linear viscous in accordance to the assumed background rock viscosity. The rheological behaviour of the model is initially linear viscous. If stresses locally exceed the yield stress ($F(\tau_{ij}$, $P, \varphi, C) > 0$), effective viscosities η are decreased following the second invariant of the strain-rate tensor $\dot{\varepsilon}^{II}$ and the yield stress σ_y until the maximum stresses are at the yield stress ($F = 0$), according to

$$\eta_{vp} = \frac{\sigma_y}{2\dot{\varepsilon}^{II}} \tag{A8}$$

where

$$\dot{\varepsilon}^{II} = \sqrt{\frac{1}{2}\dot{\varepsilon}_{ij}^2} \tag{A9}$$

and η_{vp} is the effective viscosity corrected for plasticity.

Direct plastic (Picard) iterations are simultaneous with time stepping. To ensure initial model convergence and proper initiation of shear bands, the first ~400 Picard iterations are computed with a very small time step (one year) implying a negligible amount of model displacement. The following computational time steps are also relatively short (max. 1000 years, depending on marker velocities), which warrants small material displacement per time step (<10 m) and ensures accurate treatment of plasticity and good convergence of the multigrid solver.

Appendix B. Supplementary data

Supplementary data to this article can be found online at http://dx.doi.org/10.1016/j.tecto.2014.01.003.

References

Allken, V., Huismans, R.S., Thieulot, C., 2012. Factors controlling the mode of rift interaction in brittle-ductile coupled systems: a 3D numerical study. Geochem. Geophys. Geosyst. 13.

Bahroudi, A., Koyi, H.A., 2003. Effect of spatial distribution of Hormuz salt on deformation style in the Zagros fold and thrust belt: an analogue modelling approach. J. Geol. Soc. 160, 719–733.

Baker, C., Jackson, J., Priestley, K., 1993. Earthquakes on the Kazerun line in the Zagros Mountains of Iran — strike-slip faulting within a fold-and-thrust belt. Geophys. J. Int. 115, 41–61.

Bekins, B., Mccaffrey, A.M., Dreiss, S.J., 1994. Influence of kinetics on the smectite to illite transition in the Barbados accretionary prism. J. Geophys. Res. Solid Earth 99, 18147–18158.

Bercovici, D., 1993. A simple-model of plate generation from mantle flow. Geophys. J. Int. 114, 635–650.

Bercovici, D., Ricard, Y., 2012. Mechanisms for the generation of plate tectonics by two-phase grain-damage and pinning. Phys. Earth Planet. Inter. 202, 27–55.

Bos, B., Spiers, C.J., 2000. Effect of phyllosilicates on fluid-assisted healing of gouge-bearing faults. Earth Planet. Sci. Lett. 184, 199–210.

Bos, B., Peach, C.J., Spiers, C.J., 2000. Frictional-viscous flow of simulated fault gouge caused by the combined effects of phyllosilicates and pressure solution. Tectonophysics 327, 173–194.

Braun, J., Yamato, P., 2010. Structural evolution of a three-dimensional, finite-width crustal wedge. Tectonophysics 484, 181–192.

Buiter, S.J.H., 2012. A review of brittle compressional wedge models. Tectonophysics 530, 1–17.

Buiter, S.J.H., Babeyko, A.Y., Ellis, S., Gerya, T.V., Kaus, B.J.P., Kellner, A., Schreurs, G., Yamada, Y., 2006. The numerical sandbox: comparison of model results for a shortening and an extension experiment: analogue and numerical modelling of crustal-scale processes. 253, 29–64.

Burbidge, D.R., Braun, J., 2002. Numerical models of the evolution of accretionary wedges and thrust-and-fold belts using the distinct element method (vol 148, pg 542, 2002). Geophys. J. Int. 148, 542–561.

Burg, J.P., Schmalholz, S.M., 2008. Viscous heating allows thrusting to overcome crustal-scale buckling: numerical investigation with application to the Himalayan syntaxes. Earth Planet. Sci. Lett. 274, 189–203.

Burg, J.P., Bernoulli, D., Smit, J., Dolati, A., Bahroudi, A., 2008. A giant catastrophic mud-and-debris flow in the Miocene Makran. Terra Nova 20, 188–193.

Burridge, R., Knopoff, L., 1967. Model and theoretical seismicity. Bull. Seismol. Soc. Am. 57, 341–371.

Calassou, S., Larroque, C., Malavieille, J., 1993. Transfer zones of deformation in thrust wedges — an experimental-study. Tectonophysics 221, 325–344.

Cotton, J.T., Koyi, H.A., 2000. Modeling of thrust fronts above ductile and frictional detachments: application to structures in the Salt Range and Potwar Plateau, Pakistan. Geol. Soc. Am. Bull. 112, 351–363.

Crameri, F., Schmeling, H., Golabek, G.J., Duretz, T., Orendt, R., Buiter, S.J.H., May, D.A., Kaus, B.J.P., Gerya, T.V., Tackley, P.J., 2012. A comparison of numerical surface topography calculations in geodynamic modelling: an evaluation of the sticky air' method. Geophys. J. Int. 189, 38–54.

Dahlen, F.A., 1984. Noncohesive critical Coulomb wedges — an exact solution. J. Geophys. Res. 89, 125–133.

Dahlen, F.A., Suppe, J., Davis, D., 1984. Mechanics of fold-and-thrust belts and accretionary wedges — cohesive Coulomb theory. J. Geophys. Res. 89, 87–101.

Davis, D., Engelder, T., 1985. The role of salt in fold-and-thrust belts. Tectonophysics 119, 67–88.

Davis, D., Suppe, J., Dahlen, F.A., 1983. Mechanics of fold-and-thrust belts and accretionary wedges. J. Geophys. Res. 88, 1153–1172.

Davis, T.L., Namson, J., Yerkes, R.F., 1989. A cross-section of the Los-Angeles area — seismically active fold and thrust belt, the 1987 Whittier–Narrows earthquake, and earthquake hazard. J. Geophys. Res. Solid Earth Planets 94, 9644–9664.

Di Toro, G., Han, R., Hirose, T., De Paola, N., Nielsen, S., Mizoguchi, K., Ferri, F., Cocco, M., Shimamoto, T., 2011. Fault lubrication during earthquakes. Nature 471, 494–498.

Dieterich, J.H., 1979. Modeling of rock friction.1. Experimental results and constitutive equations. J. Geophys. Res. 84, 2161–2168.

Dooley, T.P., Schreurs, G., 2012. Analogue modelling of intraplate strike-slip tectonics: a review and new experimental results. Tectonophysics 574, 1–71.

Ellis, S., Schreurs, G., Panien, M., 2004. Comparisons between analogue and numerical models of thrust wedge development. J. Struct. Geol. 26, 1659–1675.

Escartin, J., Hirth, G., Evans, B., 1997. Effects of serpentinization on the lithospheric strength and the style of normal faulting at slow-spreading ridges. Earth Planet. Sci. Lett. 151, 181–189.

Fillon, C., Huismans, R.S., van der Beek, P., 2013. Syntectonic sedimentation effects on the growth of fold-and-thrust belts. Geology 41 (1), 83–86.

Fischer, G.J., Paterson, M.S., 1989. Dilatancy during rock deformation at high-temperatures and pressures. J. Geophys. Res. Solid Earth Planets 94, 17607–17617.

Gerya, T., 2010. Introduction to Numerical Geodynamic Modelling. Cambridge University Press (345 pp.).

Gerya, T.V., 2013. Three-dimensional thermomechanical modeling of oceanic spreading initiation and evolution. Phys. Earth Planet. Inter. 214, 35–52.

Gerya, T.V., Yuen, D.A., 2003. Rayleigh–Taylor instabilities from hydration and melting propel 'cold plumes' at subduction zones. Earth Planet. Sci. Lett. 212, 47–62.

Gerya, T., Yuen, D.A., 2007. Robust characteristics method for modelling multiphase visco-elasto-plastic thermo-mechanical problems. Phys. Earth Planet. Inter. 163, 83–105.

Grando, G., McClay, K., 2007. Morphotectonics domains and structural styles in the Makran accretionary prism, offshore Iran. Sediment. Geol. 196, 157–179.

Graveleau, F., Malavieille, J., Dominguez, S., 2012. Experimental modelling of orogenic wedges: a review. Tectonophysics 1–66.

Hickman, S., Sibson, R., Bruhn, R., 1995. Introduction to special section — mechanical involvement of fluids in faulting. J. Geophys. Res. Solid Earth 100, 12831–12840.

Huismans, R.S., Buiter, S.J.H., Beaumont, C., 2005. Effect of plastic-viscous layering and strain softening on mode selection during lithospheric extension. J. Geophys. Res. Solid Earth 110.

Konstantinovskaya, E., Malavieille, J., 2011. Thrust wedges with decollement levels and syntectonic erosion: a view from analog models. Tectonophysics 502, 336–350.

Lanson, B., Sakharov, B.A., Claret, F., Drits, V.A., 2009. Diagenetic smectite-to-illite transition in clay-rich sediments: a reappraisal of X-ray diffraction results using the multi-specimen method. Am. J. Sci. 309, 476–516.

Lavier, L.L., Buck, W.R., Poliakov, A.N.B., 2000. Factors controlling normal fault offset in an ideal brittle layer. J. Geophys. Res. Solid Earth 105, 23431–23442.

Macedo, J., Marshak, S., 1999. Controls on the geometry of fold-thrust belt salients. Geol. Soc. Am. Bull. 111, 1808–1822.

Marques, F.O., Cobbold, P.R., 2006. Effects of topography on the curvature of fold-and-thrust belts during shortening of a 2-layer model of continental lithosphere. Tectonophysics 415, 65–80.

Medialdea, T., Vegas, R., Somoza, L., Vazquez, J.T., Maldonado, A., Diaz-Del-Rio, V., Maestro, A., Cordoba, D., Fernandez-Puga, M.C., 2004. Structure and evolution of the "Olistostrome" complex of the Gibraltar Arc in the Gulf of Cadiz (eastern Central Atlantic): evidence from two long seismic cross-sections. Mar. Geol. 209, 173–198.

Miyakawa, A., Yamada, Y., Matsuoka, T., 2010. Effect of increased shear stress along a plate boundary fault on the formation of an out-of-sequence thrust and a break in surface slope within an accretionary wedge, based on numerical simulations. Tectonophysics 484, 127–138.

Montesi, L.G.J., Zuber, M.T., 2003. Spacing of faults at the scale of the lithosphere and localization instability: 1. Theory. J. Geophys. Res. Solid Earth 108.

Morley, C.K., King, R., Hillis, R., Tingay, M., Backe, G., 2011. Deepwater fold and thrust belt classification, tectonics, structure and hydrocarbon prospectivity: a review. Earth Sci. Rev. 104, 41–91.

Mosar, J., 1999. Present-day and future tectonic underplating in the western Swiss Alps: reconciliation of basement/wrench-faulting and decollement folding of the Jura and Molasse basin in the Alpine foreland. Earth Planet. Sci. Lett. 173, 143–155.

Nilforoushan, F., Koyi, H.A., 2007. Displacement fields and finite strains in a sandbox model simulating a fold-thrust-belt. Geophys. J. Int. 169, 1341–1355.

Nilfouroushan, F., Pysklywec, R., Cruden, A., 2012. Sensitivity analysis of numerical scaled models of fold-and-thrust belts to granular material cohesion variation and comparison with analog experiments. Tectonophysics 526, 196–206.

Regard, V., Bellier, O., Thomas, J.C., Bourles, D., Bonnet, S., Abbassi, M.R., Braucher, R., Mercier, J., Shabanian, E., Soleymani, S., Feghhi, K., 2005. Cumulative right-lateral fault slip rate across the Zagros–Makran transfer zone: role of the Minab–Zendan fault system in accommodating Arabia–Eurasia convergence in southeast Iran. Geophys. J. Int. 162, 177–203.

Regenauer-Lieb, K., Rosenbaum, G., Weinberg, R.F., 2008. Strain localisation and weakening of the lithosphere during extension. Tectonophysics 458, 96–104.

Reiter, K., Kukowski, N., Ratschbacher, L., 2011. The interaction of two indenters in analogue experiments and implications for curved fold-and-thrust belts. Earth Planet. Sci. Lett. 302, 132–146.

Ruh, J.B., Kaus, B.J.P., Burg, J.P., 2012. Numerical investigation of deformation mechanics in fold-and-thrust belts: influence of rheology of single and multiple décollements. Tectonics 31.

Ruh, J.B., Gerya, T., Burg, J.P., 2013. High-resolution 3D numerical modeling of thrust wedges: influence of décollement strength on transfer zones. Geochem. Geophys. Geosyst. 14 (4), 1131–1155.

Ruina, A., 1983. Slip instability and state variable friction laws. J. Geophys. Res. 88, 359–370.

Rutter, E.H., 1999. On the relationship between the formation of shear zones and the form of the flow law for rocks undergoing dynamic recrystallization. Tectonophysics 303, 147–158.

Schenk, O., Gartner, K., 2004. Solving unsymmetric sparse systems of linear equations with PARDISO. Futur. Gener. Comput. Syst. 20, 475–487.

Schenk, O., Gartner, K., 2006. On fast factorization pivoting methods for sparse symmetric indefinite systems. Electron. Trans. Numer. Anal. 23, 158–179.

Schluter, H.U., Prexl, A., Gaedicke, C., Roeser, H., Reichert, C., Meyer, H., von Daniels, C., 2002. The Makran accretionary wedge: sediment thicknesses and ages and the origin of mud volcanoes. Mar. Geol. 185, 219–232.

Schmeling, H., Babeyko, A.Y., Enns, A., Faccenna, C., Funiciello, F., Gerya, T., Golabek, G.J., Grigull, S., Kaus, B.J.P., Morra, G., Schmalholz, S.M., van Hunen, J., 2008. A benchmark comparison of spontaneous subduction models—towards a free surface. Phys. Earth Planet. Inter. 171, 198–223.

Selzer, C., Buiter, S.J.H., Pfiffner, O.A., 2007. Sensitivity of shear zones in orogenic wedges to surface processes and strain softening. Tectonophysics 437, 51–70.

Simpson, G.D.H., 2006. Modelling interactions between fold-thrust belt deformation, foreland flexure and surface mass transport. Basin Res. 18, 125–143.

Simpson, G.D.H., 2009. Mechanical modelling of folding versus faulting in brittle-ductile wedges. J. Struct. Geol. 31, 369–381.

Simpson, G.D.H., 2011. Mechanics of non-critical fold-thrust belts based on finite element models. Tectonophysics 499, 142–155.

Sleep, N.H., 1995. Ductile creep, compaction, and rate and state-dependent friction within major fault zones. J. Geophys. Res. Solid Earth 100, 13065–13080.

Sommaruga, A., 1999. Decollement tectonics in the Jura foreland fold-and-thrust belt. Mar. Pet. Geol. 16, 111–134.

Stewart, M., Holdsworth, R.E., Strachan, R.A., 2000. Deformation processes and weakening mechanisms within the frictional-viscous transition zone of major crustal-scale faults: insights from the Great Glen Fault Zone, Scotland. J. Struct. Geol. 22, 543–560.

Stockmal, G.S., Beaumont, C., Nguyen, M., Lee, B., 2007. Mechanics of thin-skinned fold-and-thrust belts: insights from numerical models. Geol. Soc. Am. Spec. Pap. 433, 63–98.

Suppe, J., 1983. Geometry and kinematics of fault-bend folding. Am. J. Sci. 283, 684–721.

Tackley, P.J., 1998. Self-consistent generation of tectonic plates in three-dimensional mantle convection. Earth Planet. Sci. Lett. 157, 9–22.

Tackley, P.J., 2000. Self-consistent generation of tectonic plates in time-dependent, three-dimensional mantle convection simulations 2. Strain weakening and asthenosphere. Geochem. Geophys. Geosyst. 1.

Thielmann, M., Kaus, B.J.P., 2012. Shear heating induced lithospheric-scale localization: does it result in subduction? Earth Planet. Sci. Lett. 359, 1–13.

Tobin, H.J., Moore, J.C., Mackay, M.E., Orange, D.L., Kulm, L.D., 1993. Fluid-flow along a strike-slip-fault at the toe of the Oregon accretionary prism — implications for the geometry of frontal accretion. Geol. Soc. Am. Bull. 105, 569–582.

Tumarkina, E., Misra, S., Burlini, L., Connolly, J.A.D., 2011. An experimental study of the role of shear deformation on partial melting of a synthetic metapelite. Tectonophysics 503, 92–99.

vanDinther, Y., Gerya, T., Dalguer, L.A., Corbi, F., Funiciello, F., Mai, P.M., 2013. The seismic cycle at subduction thrusts: 2. Dynamic implications of geodynamic simulations validated with laboratory models. J. Geophys. Res. Solid Earth 118 (4), 1502–1525.

Wang, K., 2007. In: Dixon, T., Moore, J. (Eds.), Elastic and Viscoelastic Models of Crustal Deformation in Subduction Earthquake Cycles. Columbia University Press, New York.

Yamato, P., Kaus, B.J.P., Mouthereau, F., Castelltort, S., 2011. Dynamic constraints on the crustal-scale rheology of the Zagros fold belt, Iran. Geology 39, 815–818.

Yue, L.F., Suppe, J., Hung, J.H., 2005. Structural geology of a classic thrust belt earthquake: the 1999 Chi-Chi earthquake Taiwan (M-w = 7.6). J. Struct. Geol. 27, 2058–2083.

Zaleski, S., Julien, P., 1992. Numerical-simulation of Rayleigh–Taylor instability for single and multiple salt diapirs. Tectonophysics 206, 55–69.